DOT/FAA/AR-08/46

Air Traffic Organization
Operations Planning
Office of Aviation Research
and Development
Washington, DC 20591

Impact Tests of Aircraft Aluminums and Composites for Uncontained Engine Fragment Modeling

October 2008

This document is available to the U.S. public through the National Technical Information Service (NTIS), Springfield, Virginia 22161.

U.S. Department of Transportation
Federal Aviation Administration

NOTICE

This document is disseminated under the sponsorship of the U.S. Department of Transportation in the interest of information exchange. The United States Government assumes no liability for the contents or use thereof. The United States Government does not endorse products or manufacturers. Trade or manufacturer's names appear herein solely because they are considered essential to the objective of this report. This document does not constitute FAA certification policy. Consult your local FAA aircraft certification office as to its use.

This report is available at the Federal Aviation Administration William J. Hughes Technical Center's Full-Text Technical Reports page: actlibrary.act.faa.gov in Adobe Acrobat portable document format (PDF).

Technical Report Documentation Page

1. Report No.	2. Government Accession No.	3. Recipient's Catalog No.
DOT/FAA/AR-08/46		

4. Title and Subtitle	5. Report Date
IMPACT TESTS OF AIRCRAFT ALUMINUMS AND COMPOSITES FOR UNCONTAINED ENGINE FRAGMENT MODELING	October 2008
	6. Performing Organization Code
7. Author(s)	8. Performing Organization Report No.
Kevin Donovan, George Johnson, and Tarek Zohdi	
9. Performing Organization Name and Address	10. Work Unit No. (TRAIS)
University of California, Berkeley Berkeley, California 94720	11. Contract or Grant No.
12. Sponsoring Agency Name and Address	13. Type of Report and Period Covered
U.S. Department of Transportation Federal Aviation Administration Air Traffic Organization Operations Planning Office of Aviation Research and Development Washington, DC 20591	Final Report
	14. Sponsoring Agency Code ANM-100

15. Supplementary Notes

The Federal Aviation Administration Airport and Aircraft Safety R&D Division Technical Monitor was Donald Altobelli.

16. Abstract

Transport aircraft design requires that manufacturers minimize the risk of a catastrophic failure resulting from an uncontained engine failure. This happens when one of the turbine engine's rotating components fails, usually due to fatigue, and passes through the engine containment structure. While the loss of one engine is not enough to cause the complete failure of the commercial aircraft, the subsequent loss of critical components, such as the hydraulic or fuel lines, could result in losing control of the aircraft. Redundancy is a primary design feature that allows for the loss of an engine or major system without causing a catastrophic event.

Separation of redundant systems is also a vital part of the design process. In cases where a critical component is vulnerable, shielding may be used to protect the component. To reduce the weight and operating cost for shielding, lightweight materials, such as aluminum, titanium, high-strength fabric, composites, and other materials, are being considered to act as barriers against engine fragments on critical aircraft systems. In developing a barrier, it is necessary to characterize the ballistic performance of these materials, which is typically done through testing.

This report describes the tests performed at the University of California at Berkeley to aid in this characterization. In the experiments, 1/16-inch-thick 2024-T3 aluminum, 5/64-inch-thick 7075-T73 aluminum, and 8- and 16-ply unidirectional carbon fiber composite panels were impacted with 1/2-inch-diameter spheres, flat-ended cylinders, and hemispherically ended cylinders shot from a pneumatic gun. Impact curves were generated, and failure methods were observed.

The composite panels failed by fracture, delamination, and plugging, depending on conditions such as projectile velocity, projectile tip shape, and target thickness. Projectile shape also affected the amount of energy required for a projectile to pass through the aluminum plates. For all materials tested, an assumption of constant projectile energy loss, independent of initial projectile speed, seemed valid.

17. Key Words	18. Distribution Statement
Fracture, Plugging, Petalling, Delamination, Composite, Shear	This document is available to the U.S. public through the National Technical Information Service (NTIS) Springfield, Virginia 22161.

19. Security Classif. (of this report)	20. Security Classif. (of this page)	21. No. of Pages	22. Price
Unclassified	Unclassified	58	

Form DOT F1700.7 (8-72) Reproduction of completed page authorize

TABLE OF CONTENTS

			Page
EXECUTIVE SUMMARY			ix
1.	INTRODUCTION		1
	1.1	PURPOSE	1
	1.2	BACKGROUND	1
2.	EXPERIMENTAL PROCEDURE		1
	2.1	PNEUMATIC GUN SETUP	1
		2.1.1 Pneumatic Gas Gun	2
		2.1.2 Laser Velocity Measurement System	4
		2.1.3 Target Holder and Mount	5
		2.1.4 High-Speed Camera Velocity Measurement System	5
		2.1.5 Catcher Box	6
	2.2	Projectiles	7
	2.3	Impact Test Procedure	8
	2.4	Quasi-Static Load Tests	8
		2.4.1 Instron Testing Setup	8
		2.4.2 Modified Projectile and Holder	9
		2.4.3 Instron Test Procedure	11
3.	RESULTS AND DISCUSSION		11
	3.1	2024-T3 Aluminum	11
	3.2	7075-T73 Aluminum	16
	3.3	Eight-Ply Unidirectional Composite	19
	3.4	Sixteen-Ply Unidirectional Composite	22
	3.5	Angle of Incidence	25
	3.6	Instron Testing Results	26
4.	ANALYSIS		27
	4.1	Energy Analysis	27
	4.2	Shear Plugging Energy	35
	4.3	Cylinder Instron Testing	35
5.	CONCLUSIONS		36
6.	REFERENCES		37

APPENDICES

A—Camera Instructions
B—Impact Data
C—BMS 8-212 Material Data
D—Load Displacement Curves From Instron Tests

LIST OF FIGURES

Figure		Page
1	The UCB Pneumatic Gun Setup	2
2	A Schematic of the Pneumatic Gun Setup	2
3	One-Half-Inch-Diameter Spherical Projectile Calibration Curve	3
4	One-Half-Inch-Diameter Cylindrical Projectile Calibration Curve	3
5	The Flow of Nitrogen Gas From Tank to Pneumatic Gun	4
6	Close-Up of Pneumatic Gun	4
7	Laser Velocity Measurement System	5
8	Target Holder and Mount	5
9	High-Speed Camera Field of Vision	6
10	High-Speed Camera	6
11	Catcher Box	7
12	Cylindrical Projectile Dimensions	7
13	The Instron Testing Setup	9
14	Projectiles Modified for Instron Test	10
15	Collet-Like Fixture Used to Hold Projectiles During Testing	10
16	Impact Curves for 2024-T3 Aluminum	12
17	Projectile Energy Loss Curves for 2024-T3 Aluminum	13
18	2024-T3 Aluminum Damage From Spheres	14
19	2024-T3 Damage From Flat-Ended Cylinders	14
20	2024-T3 Damage From Hemispherically Ended Cylinders	15
21	Flat-Ended Cylinders Produce Larger Plugs Than Hemispherically Ended Cylinders	16
22	Impact Curves for 7075-T73 Aluminum	17

23	Projectile Energy Loss Curves for 7075-T73 Aluminum	17
24	7075-T3 Aluminum Damage From Spheres	18
25	7075-T73 Aluminum Damage From Flat-Ended Cylinders	18
26	7075-T73 Aluminum Damage From Hemispherically Ended Cylinders	19
27	Impact Curves for 8-Ply Unidirectional Composite	20
28	Projectile Energy Loss Curves for 8-Ply Unidirectional Composite	20
29	Eight-Ply Unidirectional Composite Panel Damage From Spheres	21
30	Impact Curves for 16-Ply Unidirectional Composite	22
31	Projectile Energy Loss Curves for 16-Ply Unidirectional Composite	23
32	Sixteen-Ply Unidirectional Composite Panel Damage From Spheres	24
33	Projectile Tumbling	25
34	Tearing Caused by a Tumbling Flat-Ended Cylinder	25
35	Angle of Incidence of the Cylindrical Projectile at Impact Versus Initial Projectile Velocity	26
36	Load vs Displacement Curves From Instron Testing for 2024-T3 Aluminum With a Flat-Ended Cylinder	27
37	Predicted Impact Curve for 2024-T3 Aluminum With Spheres	30
38	Predicted Impact Curve for 2024-T3 Aluminum Flat-Ended Cylinders	30
39	Predicted Impact Curve for 2024-T3 Aluminum With Hemispherically Ended Cylinders	31
40	Predicted Impact Curve for 7075-T73 Aluminum With Spheres	31
41	Predicted IMPACT Curve for 7075-T73 Aluminum With Flat-Ended Cylinders	32
42	Predicted Impact Curve for 7075-T73 Aluminum With Hemispherically Ended Cylinders	32
43	Predicted Impact Curve for 8-Ply Composite With Spheres	33
44	Predicted Impact Curve for 8-Ply Composite With Hemispherically Ended Cylinders	33

45 Predicted Impact Curve for 16-Ply Composite With Spheres 34

46 Predicted Impact Curve for 16-Ply Composite With Hemispherically Ended Cylinders 34

LIST OF TABLES

Table		Page
1	2024-T3 Aluminum Nominal Material Properties	11
2	7075-T73 Aluminum Nominal Material Properties	16
3	Predicted Ballistic Limits Based on the Assumption of Constant Projectile Energy Loss	28
4	Estimated Work Required to Create Shear Plugs in Aluminums With Flat-Ended Cylinders	35
5	Estimated Work Required for Cylindrical Sections of Projectiles to Pass Through Target Plates	36

EXECUTIVE SUMMARY

Transport aircraft design requires that manufacturers minimize the risk of a catastrophic failure resulting from an uncontained engine failure. This happens when one of the turbine engine's rotating components fails, usually due to fatigue, and passes through the engine containment structure. While the loss of one engine is not enough to cause the complete failure of the commercial aircraft, the subsequent loss of critical components, such as the hydraulic or fuel lines, could result in the loss of control of the aircraft. Redundancy is a primary design feature that allows for the loss of an engine or major system without causing a catastrophic event.

Separation of redundant systems is also a vital part of the design process. In cases where a critical component is vulnerable, shielding may be used to protect the component. To reduce the weight and operating cost for shielding, lightweight materials, such as aluminum, titanium, high-strength fabric, composites, and other materials, are being considered to act as barriers against engine fragments on critical aircraft systems. In developing a barrier, it is necessary to characterize the ballistic performance of these materials, which is typically done by testing.

This report describes the tests performed at the University of California at Berkeley to aid in this characterization. In the experiments, 1/16-inch-thick 2024-T3 aluminum, 5/64-inch-thick 7075-T73 aluminum, and 8- and 16-ply unidirectional carbon fiber composite panels were impacted with 1/2-inch-diameter spheres, flat-ended cylinders, and hemispherically ended cylinders shot from a pneumatic gun. Impact curves were generated, and failure methods were observed.

The composite panels failed by fracture, delamination, and plugging, depending on conditions such as projectile velocity, projectile tip shape, and target thickness. Projectile shape also affected the amount of energy required for a projectile to pass through the aluminum plates. For all materials tested, an assumption of constant projectile energy loss, independent of initial projectile speed, seemed valid.

1. INTRODUCTION.

1.1 PURPOSE.

The objectives of the experiments presented in this report included the impact characterization of several aircraft materials, the determination of the effect of projectile shape on projectile energy loss, and the characterization of tumbling cylindrically shaped projectiles. Plates of 1/16-inch-thick 2024-T3 aluminum, 5/64-inch-thick 7075-T73 aluminum, and 8- and 16-ply unidirectional carbon fiber composite panels were impacted with projectiles: 1/2-inch-diameter spheres, flat-ended cylinders, and hemispherically ended cylinders. For each combination of material and projectile shape, an impact curve composed of initial and residual projectile velocity was plotted, which determined the ballistic limit and energy loss. The ballistic limit is the speed above which a projectile will pass completely through a target, and below which it will not. The angle of incidence was also measured for each shot using two cylindrically shaped projectiles in an attempt to determine a trend. In addition to the ballistic impact tests, low-speed friction tests were conducted to characterize the contact friction of different shaped projectiles as they passed through the targets.

1.2 BACKGROUND.

It is possible that airplane turbine engine rotating components may fail in use. If high-energy fragments exit the engine containment, they may penetrate the airplane fuselage and damage critical components such as fuel and hydraulic lines. In this rare case, an airplane that may otherwise be able to land with one failed engine could suffer additional system failures resulting in higher risk. To prevent engine failures from becoming catastrophic, fragment-shielding systems are being developed to protect critical aircraft systems. Fragment impact data and characterization of materials for these shields and other aircraft materials need to be acquired to allow for computational modeling.

Under the Federal Aviation Administration Airworthiness Assurance Program Center of Excellence and the Aircraft Catastrophic Failure Prevention Program, the University of California at Berkeley (UCB) investigated several different materials as barriers for engine fragments from uncontained turbine engine failures in commercial aircraft. UCB's role was to conduct ballistic impact tests on these materials and to develop a computational model focused on the multiscale nature of the fabric material. This report summarizes a portion of the tests conducted.

2. EXPERIMENTAL PROCEDURE.

2.1 PNEUMATIC GUN SETUP.

All impact tests were performed using a pneumatic gun setup consisting of a nitrogen gas gun, a laser velocity measurement system, a target holder and mount, a high-speed camera velocity measurement system, and a catcher box. A photograph of the setup is shown in figure 1, and a schematic of the setup is shown in figure 2.

Figure 1. The UCB Pneumatic Gun Setup

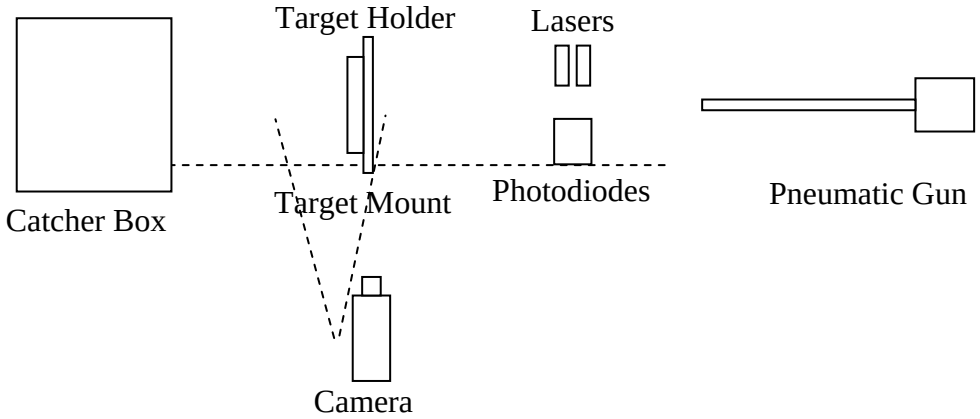

Figure 2. A Schematic of the Pneumatic Gun Setup

2.1.1 Pneumatic Gas Gun.

All impact tests were performed with a high-pressure pneumatic gun that used compressed industrial nitrogen. A regulator valve attached to the nitrogen tank allowed for pressures of 25 to 1500 psi. Pressures of approximately 1500 psi resulted in maximum speeds of nearly 800 ft/s for steel spherical projectiles of 0.018 lb (8.3 g) mass and 600 ft/s for two types of steel cylindrical projectiles of 0.082 lb (37.1 g) mass. Nitrogen pressure versus projectile velocity calibration curves for the spherical and flat-ended cylindrical projectiles are shown in figures 3 and 4, respectively. For this series of tests, the gun barrel was approximately 3 feet long with a 0.508-inch inside diameter. This diameter resulted in a relatively large gap of 0.004 inch around 0.500-inch-diameter projectiles, which could have allowed more rotation of the projectile upon exiting the barrel. An exterior trigger controlled a solenoid valve between a breech pressure chamber and the gun barrel, allowing for firing of the gun when the pressure was released. A diagram of gas flow is shown in figure 5. A close-up view of the pneumatic gun is shown in figure 6.

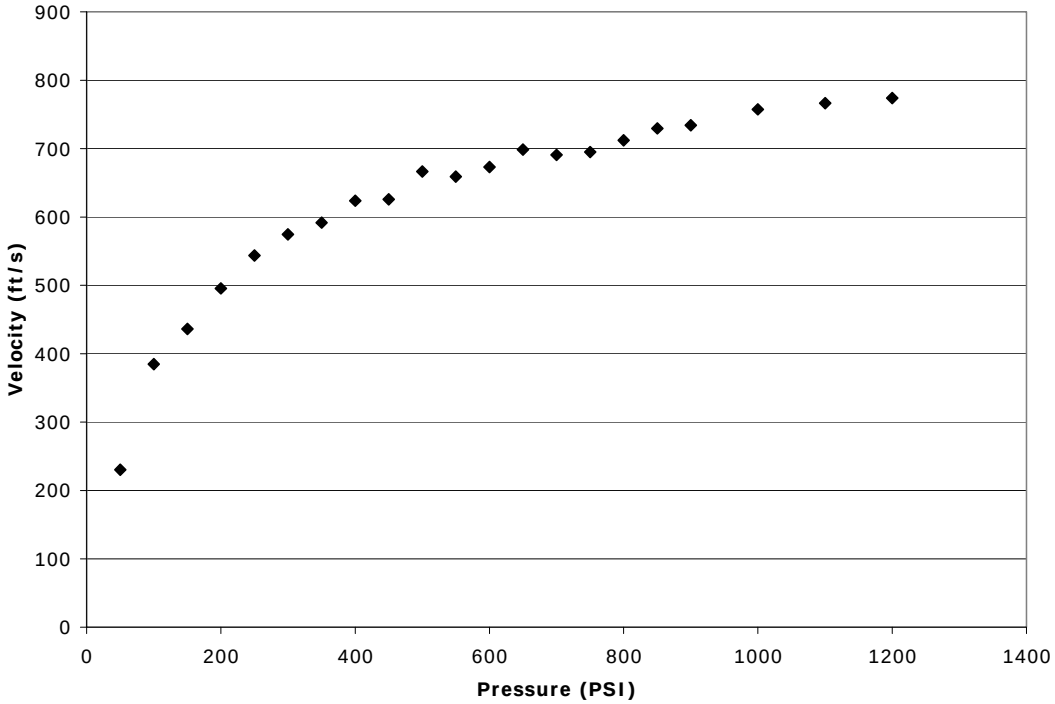

Figure 3. One-Half-Inch-Diameter Spherical Projectile Calibration Curve

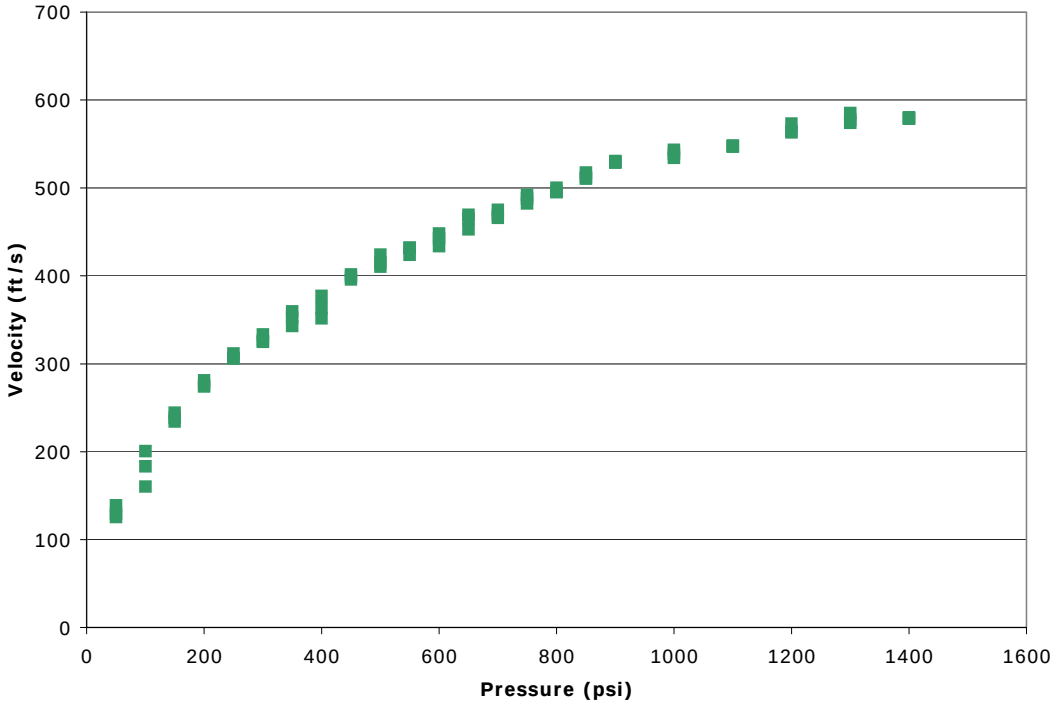

Figure 4. One-Half-Inch-Diameter Cylindrical Projectile Calibration Curve

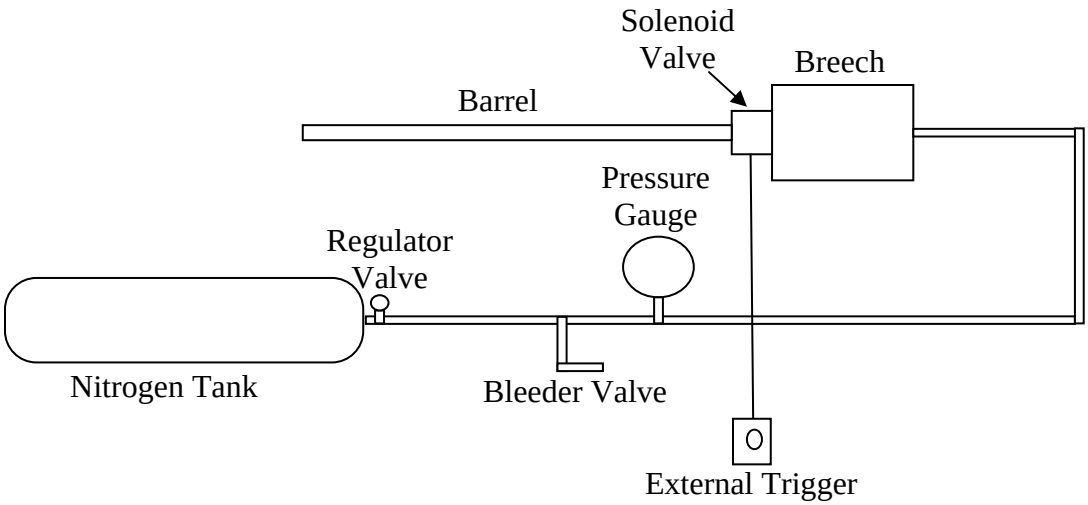

Figure 5. The Flow of Nitrogen Gas From Tank to Pneumatic Gun

Figure 6. Close-Up of Pneumatic Gun

2.1.2 Laser Velocity Measurement System.

The laser velocity measurement system, used to acquire the initial projectile velocity, consisted of two Uniphase helium-neon lasers and two Sharp IS489 photodiode light detectors. The lasers, which were positioned 2.5 inches apart, were focused at the light detectors. When the projectile passed through each laser beam, a Hewlett Packard 53131A Universal Counter would detect a voltage drop in the corresponding photodiode circuit. Projectile velocity was calculated using the time between voltage drops. The velocity measurement system is shown in figure 7.

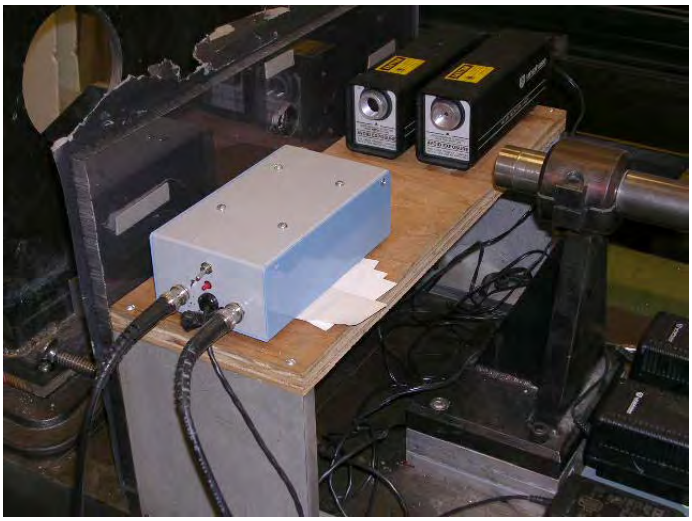

Figure 7. Laser Velocity Measurement System

2.1.3 Target Holder and Mount.

All targets were secured between two 1/2-inch-thick steel plates; both plates were 14 by 14 inches with 10- by 10-inch openings cut out of the center. Four steel bolts, tightened by hand and located at each corner of the holder, were used to hold the plates together.

The target holder was mounted using a steel angle with a 6-inch-diameter hole to allow the projectile to pass through. The holder was secured to the mount using four C-clamps, one at each corner, though 1/2-inch spacers were used to prevent direct contact between the mount and holder. The target mount was attached to the steel table using four screws. The target mount and holder are shown in figure 8.

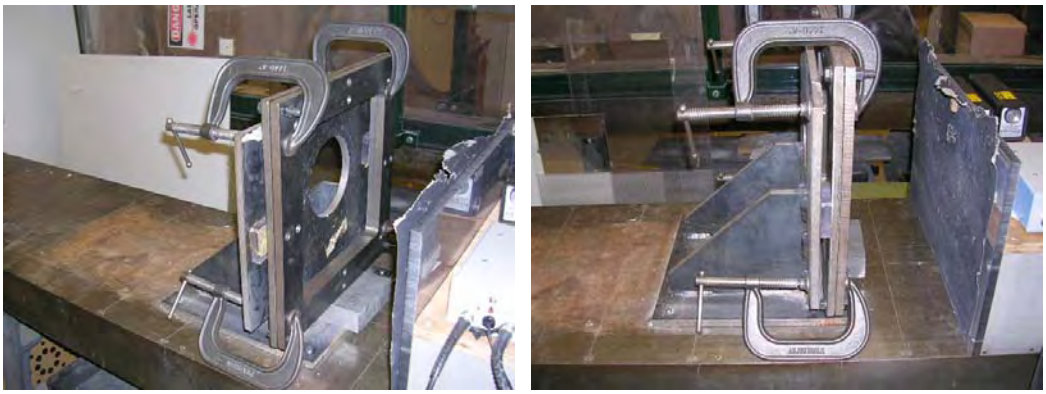

Figure 8. Target Holder and Mount

2.1.4 High-Speed Camera Velocity Measurement System.

Residual projectile velocity, as well as cylindrical projectile angle of incidence at impact, was measured using a Phantom v4.2 high-speed camera [1] with a Computar TV zoom lens. With the camera situated on a tripod approximately 5 feet perpendicular to and 1 foot above the path

of the projectile, a field of view 6 inches ahead of and 17 inches behind the target was possible. Two high-intensity lamps were used to illuminate the field of vision, which is shown in figure 9. Projectile shots were recorded at 10,000 frames per second for 3.3 seconds, 0.82 second of which are before the shot is triggered. Recordings were analyzed using Phantom Camera Control Software, allowing for determination of projectile angle of incidence (in one plane only) and residual velocity. A detailed camera use procedure can be found in appendix A. The high-speed camera is shown in figure 10.

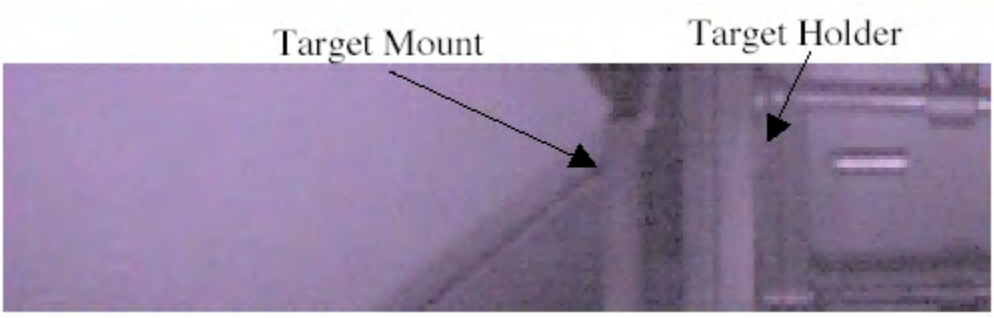

Figure 9. High-Speed Camera Field of Vision

Figure 10. High-Speed Camera

2.1.5 Catcher Box.

The catcher box consisted of a wooden box filled with Zylon® sheets and backed by a 1/2-inch-thick steel plate. After passing through the target, projectiles would be stopped by the catcher box to prevent ricocheting around the laboratory. The catcher box is shown in figure 11.

Figure 11. Catcher Box

2.2 PROJECTILES.

Three different projectiles were used in the tests: spheres, flat-ended cylinders, and hemispherically ended cylinders. The spherical projectiles were 1/2-inch-diameter chrome steel bearing balls with a mass of 0.018 lb (8.3 g). The two cylindrical projectile types were machined from 1/2-inch-diameter steel drill rod; all had a mass of 0.082 lb (37.1 g) to show the differences in material damage between the different tip shapes. Dimensions of the cylindrical projectiles are shown in figure 12.

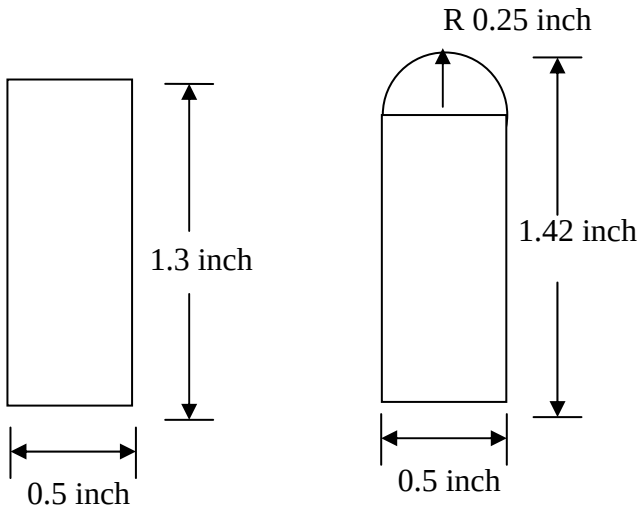

Figure 12. Cylindrical Projectile Dimensions

2.3 IMPACT TEST PROCEDURE.

The following test procedure was followed for each pneumatic gun test:

1. The 12- by 12-inch precut target was placed in the target holder, with care taken to ensure the target was centered in the holder plates.

2. The target holder was placed on the front of the target mount using C-clamps. A shim was used below the target holder to adjust the holder height ensuring the projectile hits the center of the target.

3. The projectile was loaded into the breech of the gun.

4. The universal counter was set to properly determine the time required for the projectile to pass both laser beams.

5. The pressure in the breech chamber was set using the nitrogen tank's regulator valve. After the desired pressure is reached, the regulator valve was closed.

6. The high-speed camera was set to record, waiting for the exterior trigger. The high-intensity lamps were turned on.

7. The exterior trigger was pressed.

8. The recorded shot was analyzed using the Phantom software.

2.4 QUASI-STATIC LOAD TESTS.

2.4.1 Instron Testing Setup.

The objective of these experiments was to explain the extra energy loss in the ballistic impact tests experienced by the flat-tipped cylindrical projectiles relative to spherical-tipped cylindrical projectiles. To estimate the amount of work (amount of energy transferred by force) required to "push" cylindrical projectiles through an existing target plate hole, an Instron machine was used. In the setup, the Instron machine pressed a hollow pipe down on the target plate, which was resting on top of a slightly modified projectile. The machine force was continued until the projectile had passed through the plate. A photograph of the setup is shown in figure 13.

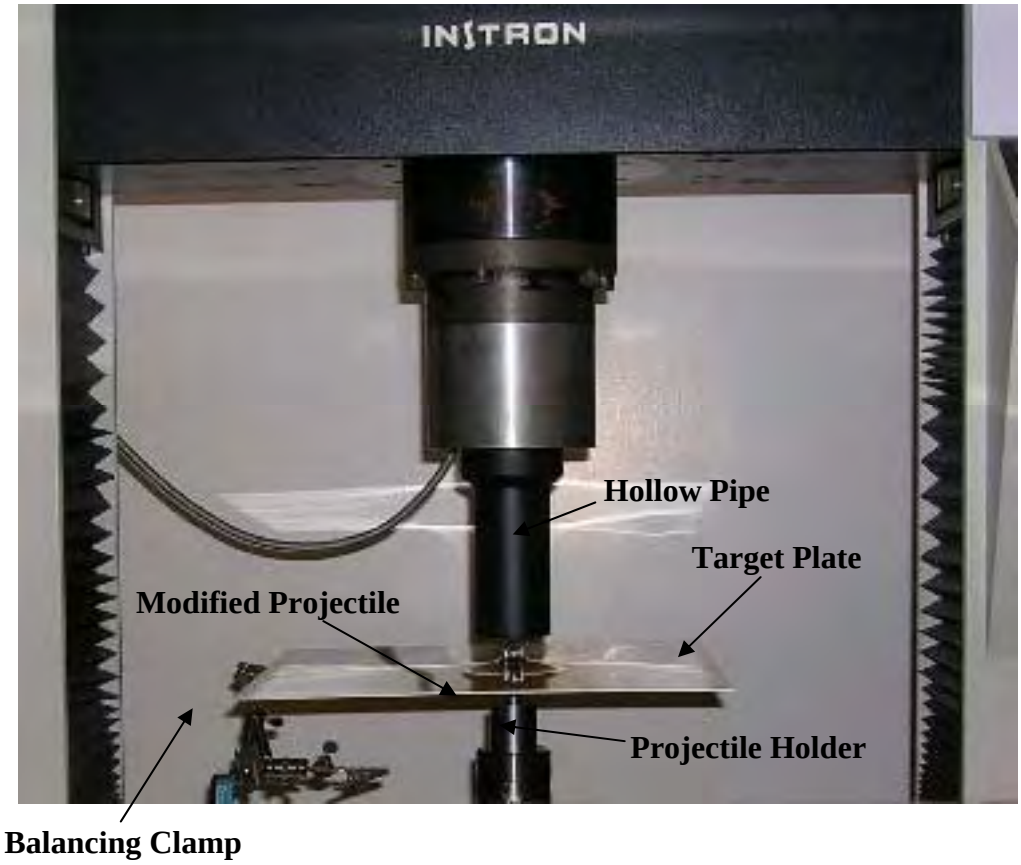

Figure 13. The Instron Testing Setup

2.4.2 Modified Projectile and Holder.

Modified cylindrical projectiles were used for the Instron tests. While the end that would impact the target plate retained the same shape and dimensions, the back end was tapered to a 3/8-inch diameter. This tapered end sat in a collet-like fixture that acted as a projectile holder. The tapering allowed the target plate to be easily removed after it had been pushed below the 1/2-inch-diameter section of the projectile. The modified projectiles are shown in figure 14. A projectile positioned in the holder is shown in figure 15.

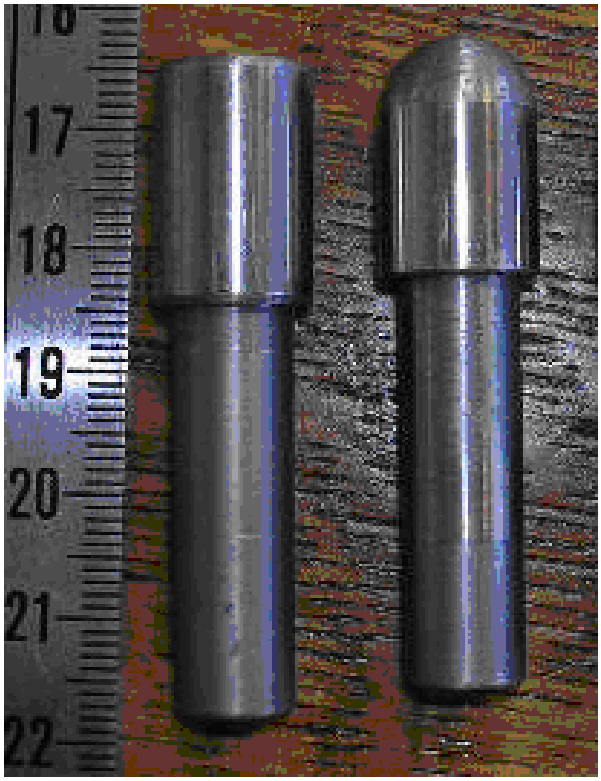

Figure 14. Projectiles Modified for Instron Test
(Note: Scales shown in all the figures are in cm.)

Figure 15. Collet-Like Fixture Used to Hold Projectiles During Testing

2.4.3 Instron Test Procedure.

The following test procedure was followed for each Instron test:

1. Affix projectile in holder.
2. Place target plate on projectile.
3. Use balancing clamp to ensure proper alignment of target plate.
4. Start Instron moving downward at a rate of 1.0 inch/min.
5. Continue until plate passes tapered section of projectile and falls downward.
6. Extract load versus displacement curve.

3. RESULTS AND DISCUSSION.

3.1 2024-T3 ALUMINUM.

Precut 12- by 12-inch, 1/16-inch 2024-T3 aluminum alloy plates were used as targets for these impact tests. Material properties for the alloy are given in table 1.

Table 1. 2024-T3 Aluminum Nominal Material Properties [2]

Ultimate Tensile Strength	Yield Strength	Elongation at Break	Shear Modulus	Density
483 MPa	345 MPa	18%	28 GPa	2.78 g/cc
70 ksi	50 ksi	18%	4060 ksi	0.1 lb/in^3

The 2024-T3 aluminum ballistic curves, which contain residual versus initial projectile velocity, are shown in figure 16. All projectile shapes are included.

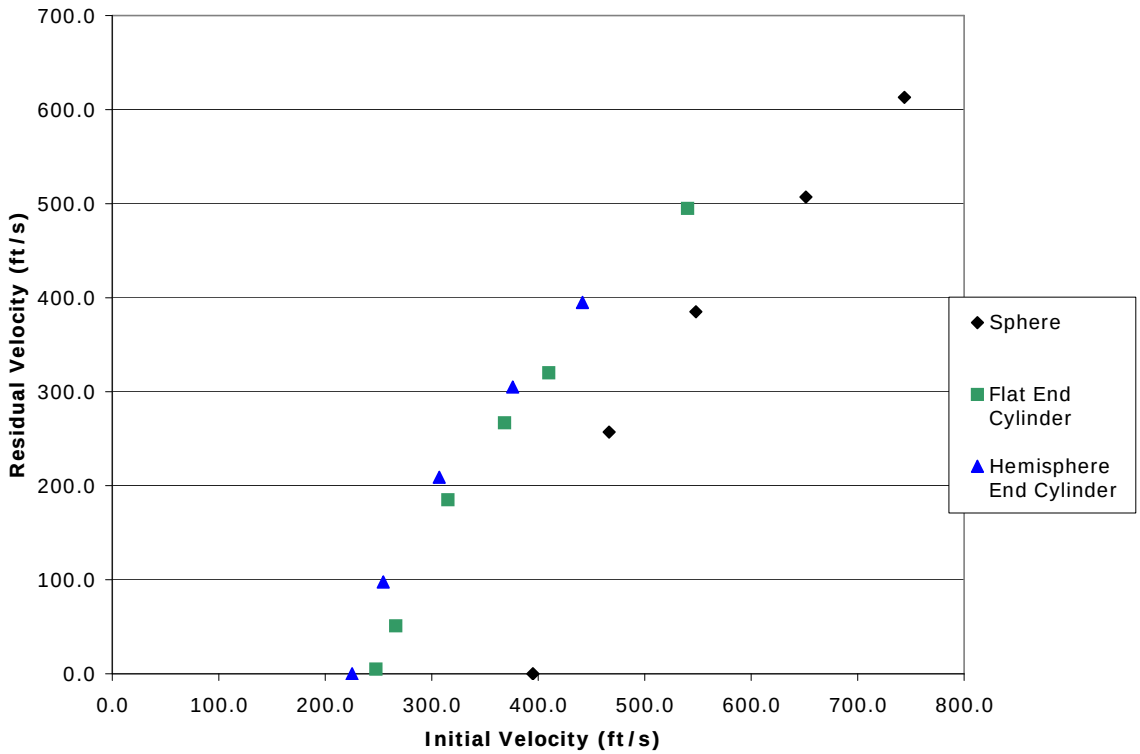

Figure 16. Impact Curves for 2024-T3 Aluminum

The ballistic limit is 393 ±5 ft/s for spherical projectiles, 249 ±5 ft/s for flat-ended cylindrical projectiles and 226 ±5 ft/s for hemispherically ended cylindrical projectiles. It must be remembered that the spherical projectiles were much lighter than the cylindrical projectiles, and thus resulted in higher ballistic limits due to the mass differences. Additional impact data is included in appendix B.

The amount of energy lost by the projectile versus the initial energy of the projectile is shown in figure 17. Lines showing a given percentage of energy loss are also included.

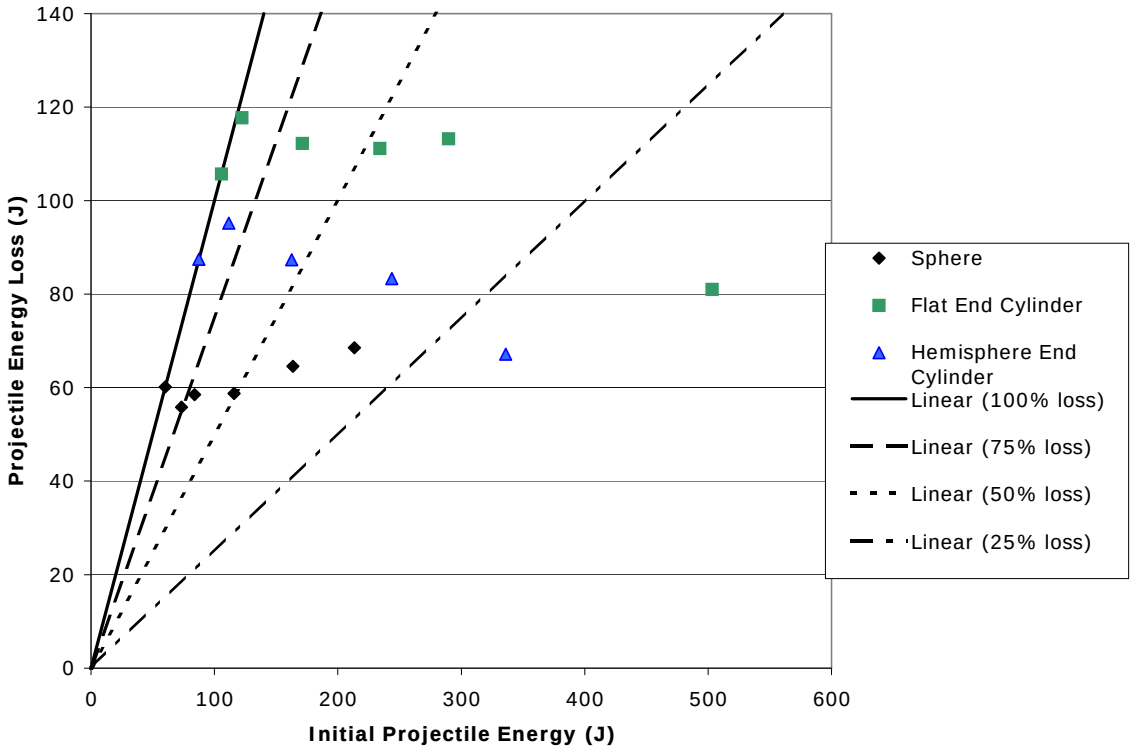

Figure 17. Projectile Energy Loss Curves for 2024-T3 Aluminum

Front and back views of a number of target plates after impact are shown in figures 18-20. Also included are initial projectile velocity, the number of petals formed, and the distance between the back face of a target plate and the tip of a petal. Petals are caused by radial cracking of material around the point of impact. Distances and the numbers of petals are not included for flat-ended cylindrical projectiles as failure with these projectiles occurred due to shear plugging only. Shear plugging occurs when the material around the point of impact is sheared, resulting in a "plug" of target material.

Initial Velocity (ft/s)	456	548	745
Petal Deformation (inch)	0.31	0.24	0.20
Number of Petals	5	6	7
Front	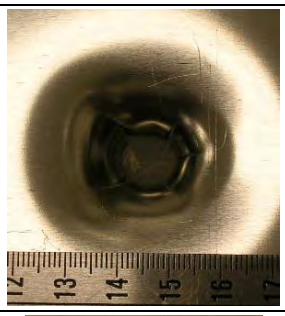	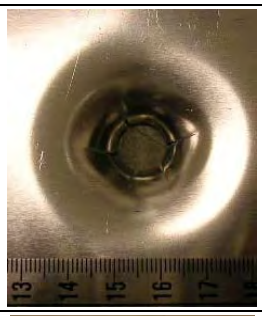	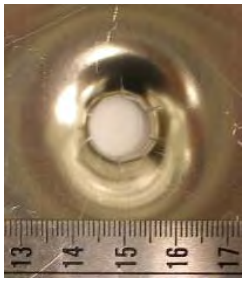
Back	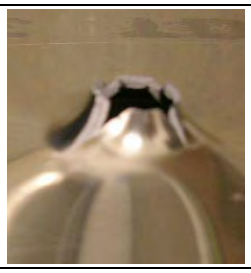	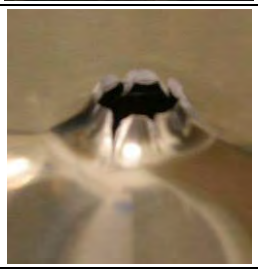	

Figure 18. 2024-T3 Aluminum Damage From Spheres

Initial Velocity (ft/s)	367	538
Front	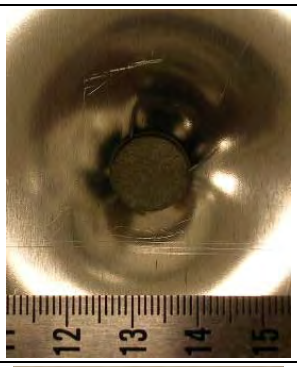	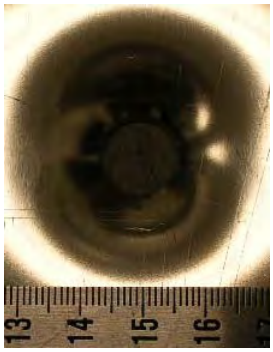
Back		

Figure 19. 2024-T3 Damage From Flat-Ended Cylinders

Initial Velocity (ft/s)	256	443	531
Petal Deformation (inch)	0.35	0.28	0.24
Number of Petals	4	5	6
Front	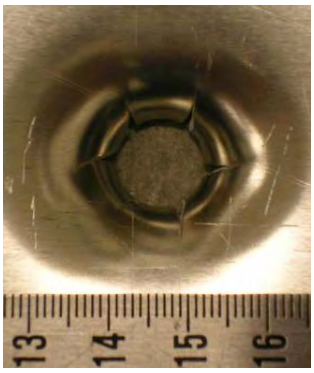	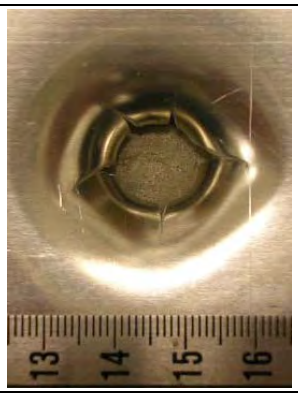	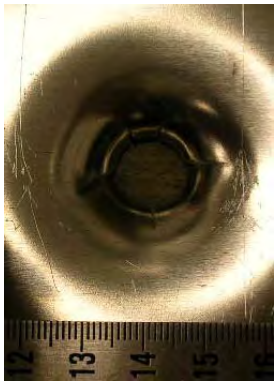
Back	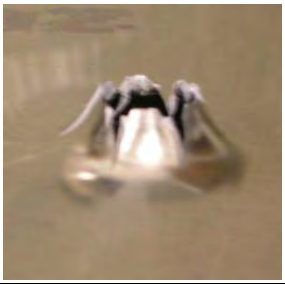		

Figure 20. 2024-T3 Damage From Hemispherically Ended Cylinders

Using flat-ended cylinder projectiles caused shear plugging of the target plate but little petalling, with higher projectile velocities yielding larger plugs. The plugs caused by flat-ended cylinders were larger than those caused by hemispherically ended projectiles because flat-ended cylinders have the largest region of initial impact, and thus, the largest area to shear around. A comparison of the plug size caused by different projectile shapes is shown in figure 21.

Spherical and hemispherically ended cylinder projectiles caused both shear plugging and petalling. When the projectile first impacted the target, a plug was sheared off. Once again, a higher initial velocity created a larger plug. Afterwards, the projectile pushed its way through the hole left by plugging, which caused petalling. Petal deformation decreased with increasing projectile velocity because with a larger plug there was less to deform.

No matter the shape of the projectile, the hole left after penetration was smaller in diameter than the projectile. This is due to some of the deformation being elastic. After the projectile passes through the target, the material springs back.

Figure 21. Flat-Ended Cylinders Produce Larger Plugs Than Hemispherically Ended Cylinders

3.2 7075-T73 ALUMINUM.

Precut 12- by 12-inch, 5/64-inch-thick 7075-T73 aluminum alloy plates were used as targets for these impact tests. Material properties for the alloy are given in table 2.

Table 2. 7075-T73 Aluminum Nominal Material Properties [3]

Ultimate Tensile Strength	Yield Strength	Elongation at Break	Shear Modulus	Density
505 MPa	435 MPa	13%	26.9 GPa	2.81 g/cc
73.2 ksi	63.1 ksi	13%	3900 ksi	0.102 lb/in^3

The 7075-T73 aluminum ballistic curves are shown below in figure 22. All projectile shapes are included.

The ballistic limit is 492 ±5 ft/s for sphere projectiles, 289 ±5 ft/s for flat-ended cylinder projectiles, and 275 ±5 ft/s for hemispherically ended cylinder projectiles. The amount of energy lost by the projectile versus the initial energy of the projectile is shown in figure 23. Lines showing a given percentage energy loss are also included.

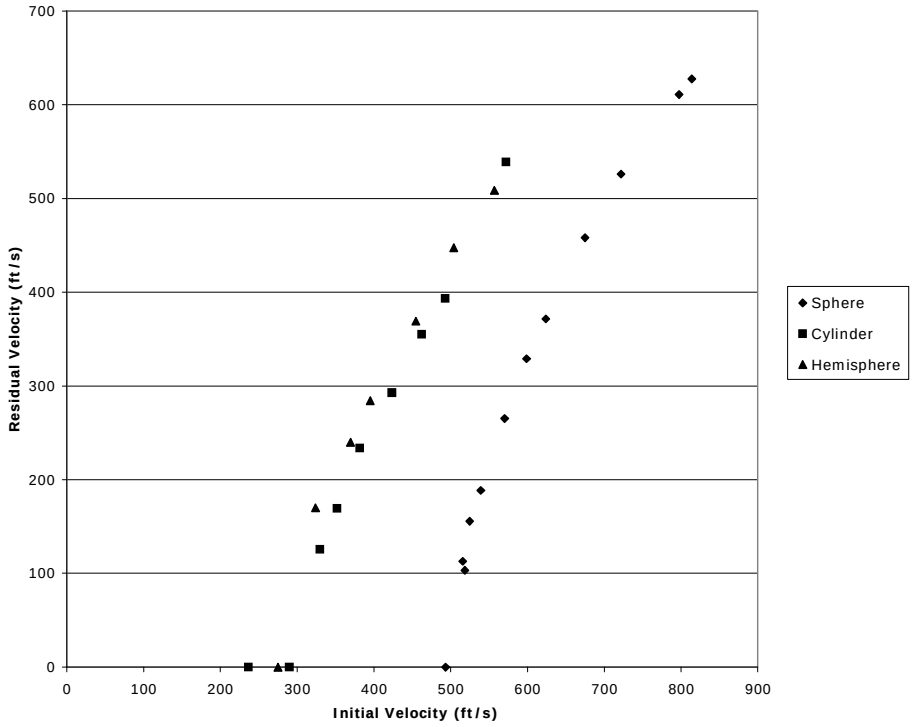

Figure 22. Impact Curves for 7075-T73 Aluminum

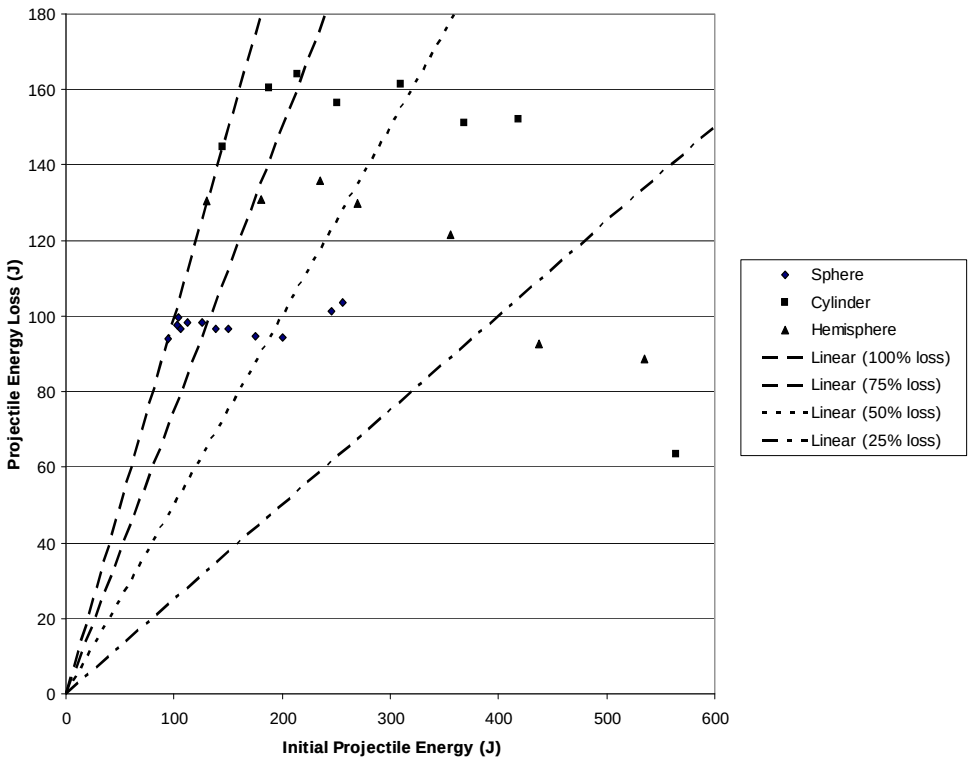

Figure 23. Projectile Energy Loss Curves for 7075-T73 Aluminum

Views of representative target plates after impact, as well as initial projectile velocity and a measure of petalling, are shown in figures 24-26.

Initial Velocity (ft/s)	492	676	813
Petal Deformation (inch)	0.35	0.28	0.24
Number of Petals	5	6	5
Front	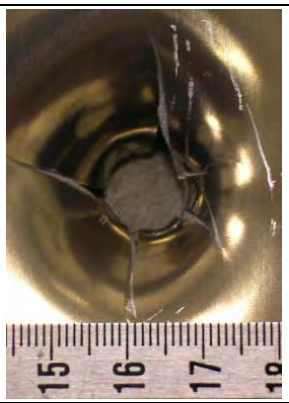	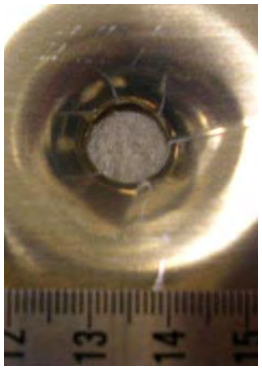	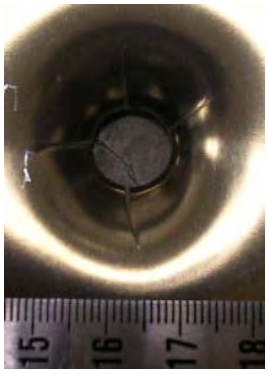
Back			

Figure 24. 7075-T3 Aluminum Damage From Spheres

Initial Velocity (ft/s)	423	571
Front	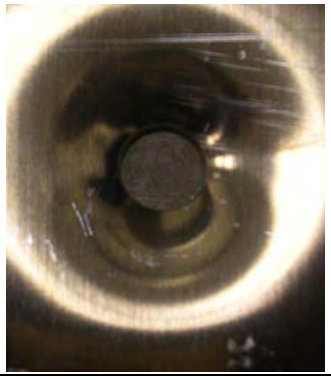	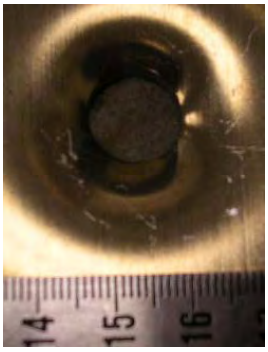
Back	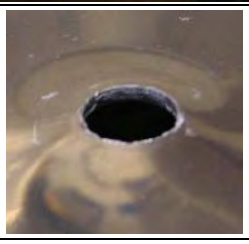	

Figure 25. 7075-T73 Aluminum Damage From Flat-Ended Cylinders

Initial Velocity (ft/s)	35	394	439
Petal Deformation (inch)	0.35	0.35	0.31
Number of Petals	5	4	4
Front	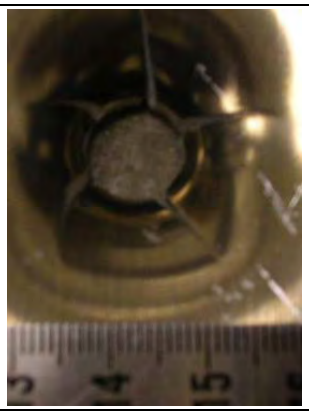	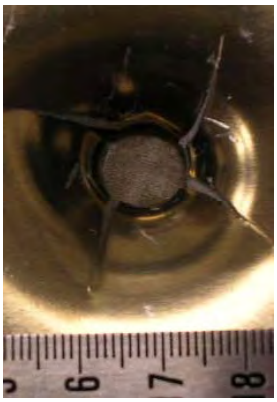	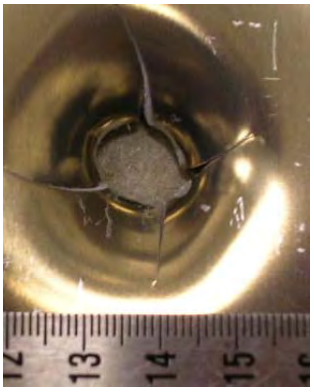
Back	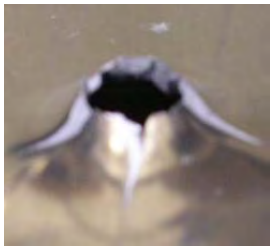		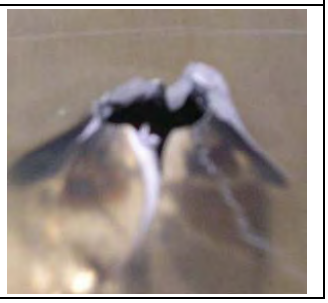

Figure 26. 7075-T73 Aluminum Damage From Hemispherically Ended Cylinders

Deformation of the 7075-T73 target plates after impact is quite similar to the deformation of 2024-T3 plates. Flat-ended cylinders caused shear plugging with no petalling. Spheres and hemispherically ended cylinders caused shear plugging, followed by petalling. As with 2024 aluminum, flat-ended cylinders resulted in the largest plugs followed by spheres and hemispherically ended cylinders.

Of note, tumbling the flat-ended cylinders sometimes resulted in tearing of the aluminum, as opposed to just shear plugging. This tearing did not seem to have an effect on energy loss in either 2024-T3 or 7075-T73. Further discussion is found in section 3.5 on angle of incidence.

3.3 EIGHT-PLY UNIDIRECTIONAL COMPOSITE.

Boeing-supplied BMS 8-212 unidirectional composite panels cut to 12 by 12 inches were used as target plates. The panel lay-up consisted of eight 0° plies; overall panel thickness varied from 0.04 to 0.08 inch. The 8-ply composite impact curves are shown in figure 27. More information about BMS 8-212 composite material is provided in appendix C. All projectile shapes are included except flat-ended cylinders. Composite panels were not impacted with flat-ended cylinders because of the unknown effect cylinder tumbling would have on damage.

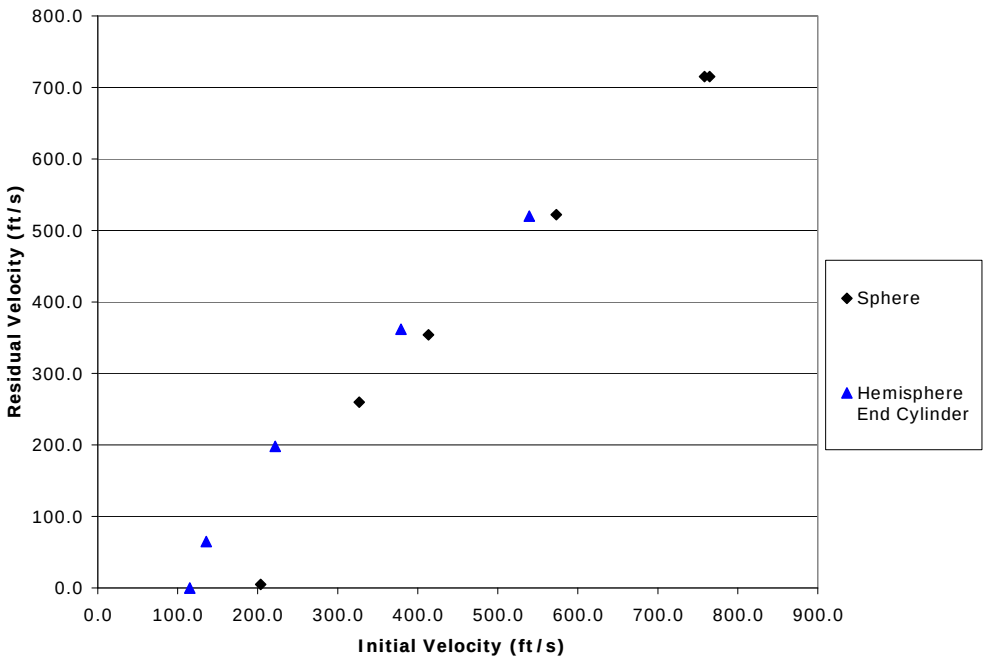

Figure 27. Impact Curves for 8-Ply Unidirectional Composite

The ballistic limit is 203 ±5 ft/s for spheres and 115 ±5 ft/s for hemispherically ended cylinders. The amount of energy lost by the projectile versus the initial energy of the projectile is shown in figure 28. The lines in figure 28 show a given percentage energy loss.

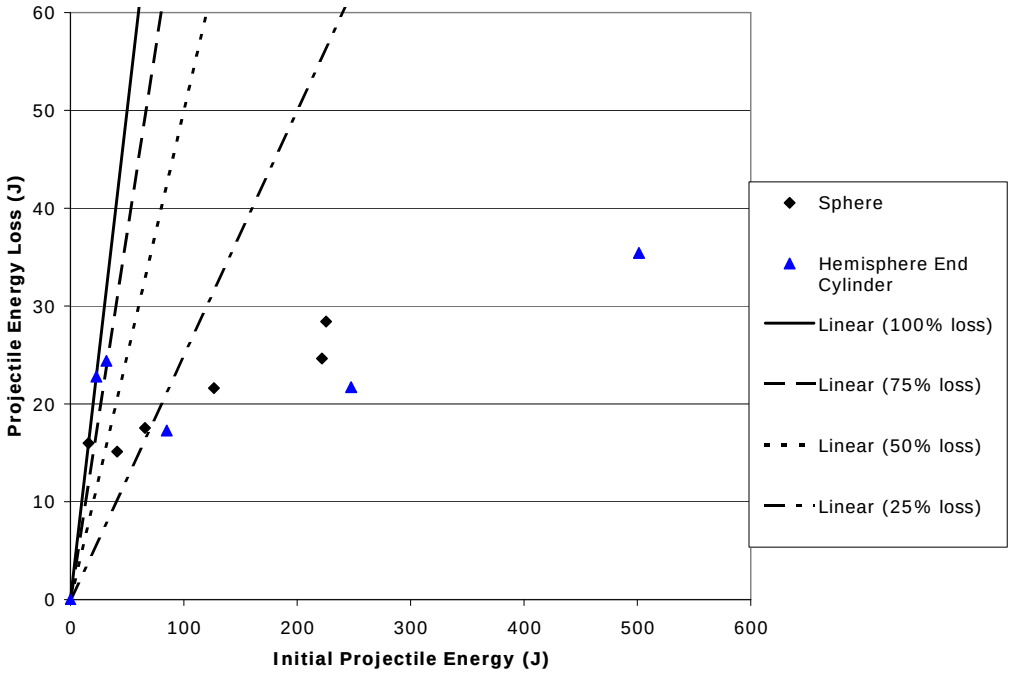

Figure 28. Projectile Energy Loss Curves for 8-Ply Unidirectional Composite

Front and back views of representative panels before and after impact, as well as initial projectile velocities, are shown in figure 29. Unlike the aluminum plates tested, different projectile shapes did not seem to produce different types of panel damage. As such, the damage due to spherically shaped projectiles are shown.

203 ft/s front	
203 ft/s back	
413 ft/s front	
413 ft/s back	
758 ft/s front	
758 ft/s back	

Figure 29. Eight-Ply Unidirectional Composite Panel Damage From Spheres

At the highest speeds, panel damage was localized to the region of impact. At the front of the panel, there was some shear plugging with a hole in the shape of the projectile. At the back, the fibers were broken normal to the fiber direction and were delaminated as the projectile pushed its way through. As velocity decreased to mid-range, shear plugging was no longer observed, and

the damage appeared to be less localized. Instead, fibers at the front of the panel were broken at the point of impact normal to the fiber direction and delaminated. This breaking and delamination continued to the back of the panel. As speeds decreased, delamination spread, moving closer to the outer edges of the panel. At low speeds near the ballistic limit, the projectiles broke very few fibers and caused little to no delamination. Rather, the panels fractured along the fiber direction starting from the point of impact and moving outward, usually to the outer edges of the panels, causing the panels to split.

3.4 SIXTEEN-PLY UNIDIRECTIONAL COMPOSITE.

Boeing-supplied BMS 8-212 unidirectional composite panels cut to 12 by 12 inches were used as target plates. The panel lay-up consisted of sixteen 0° plies; overall panel thickness varied from 0.12 to 0.16 inch. The 16-ply composite ballistic curves are shown in figure 30. All projectile shapes are included except flat-ended cylinders.

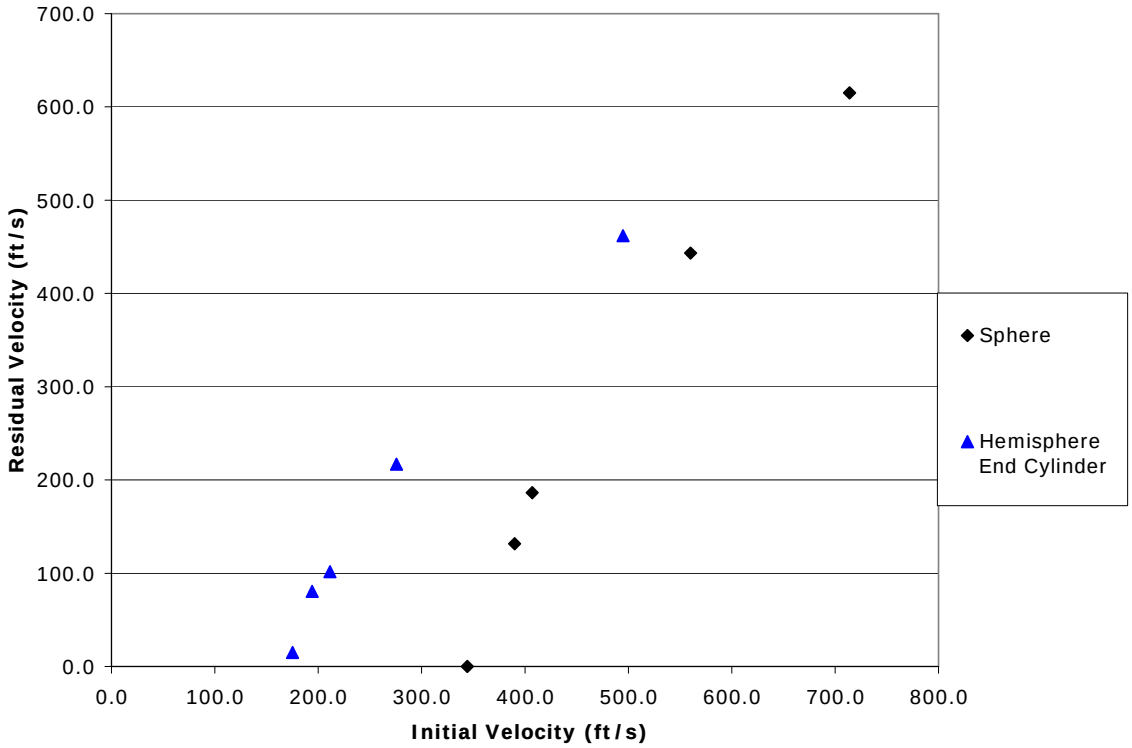

Figure 30. Impact Curves for 16-Ply Unidirectional Composite

The ballistic limit is 345 ±5 ft/s for spheres, and 170 ±5 ft/s for hemispherically ended cylinders. The amount of energy lost by the projectile versus the initial energy of the projectile is shown in figure 31. The lines in figure 31 show a given percentage energy loss.

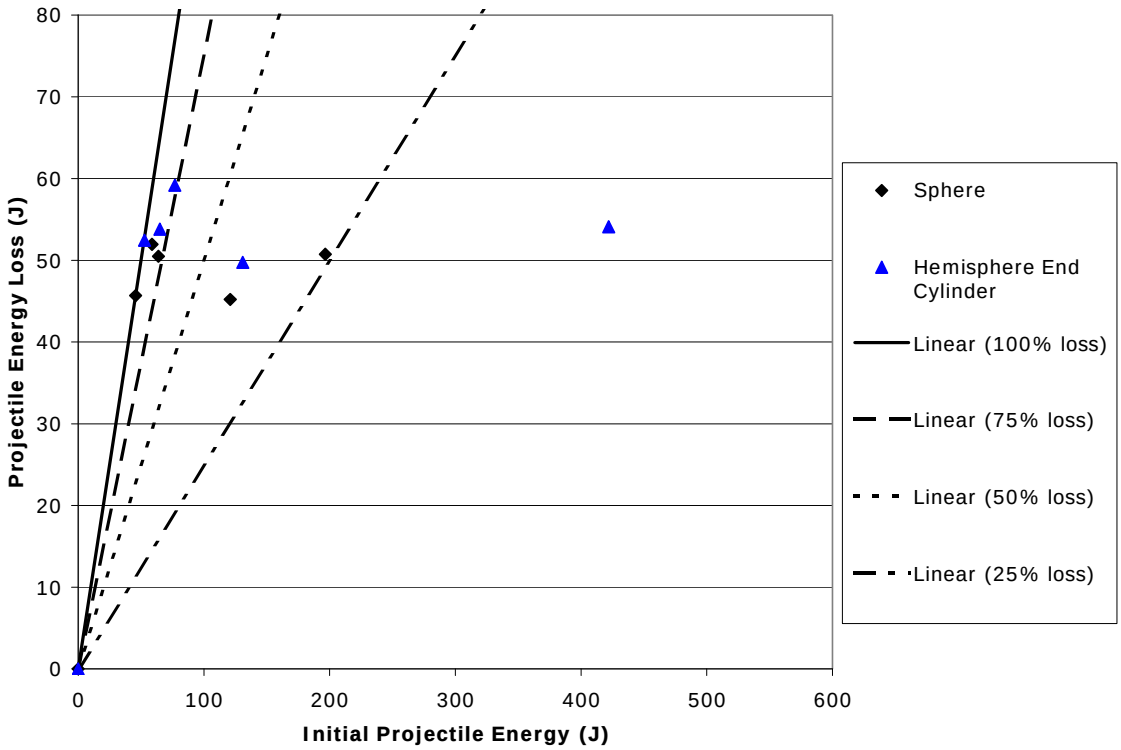

Figure 31. Projectile Energy Loss Curves for 16-Ply Unidirectional Composite

Front and back views of representative panels before and after impact, as well as initial projectile velocities, are shown in figure 32. Like the 8-ply unidirectional composite panels, different projectile shapes did not seem to produce different types of panel damage. Once again, only photographs of damage due to spherical-shaped projectiles are shown.

344 ft/s front	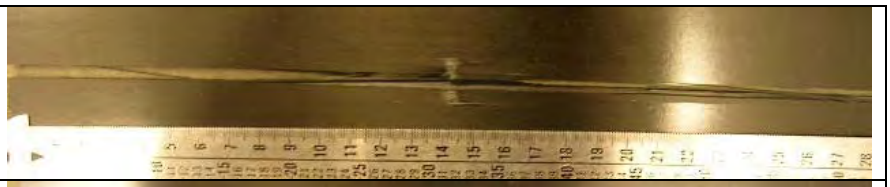
344 ft/s back	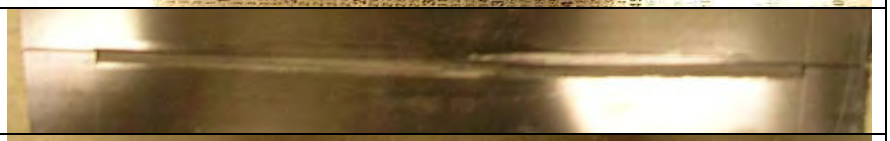
407 ft/s front	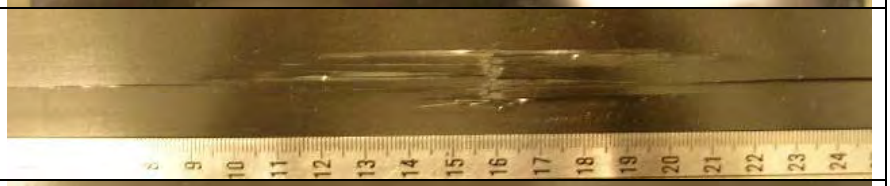
407 ft/s back	
715 ft/s front	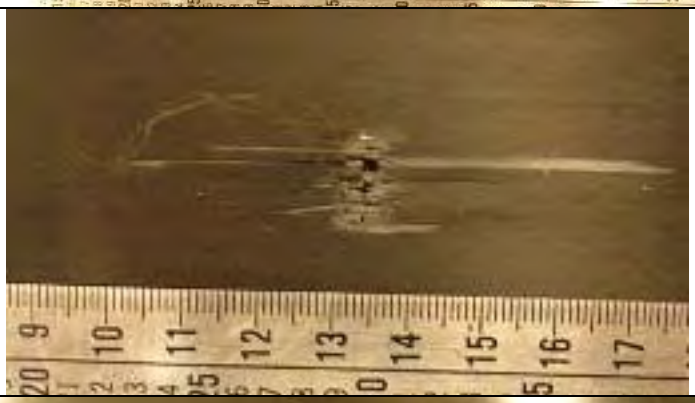
715 ft/s back	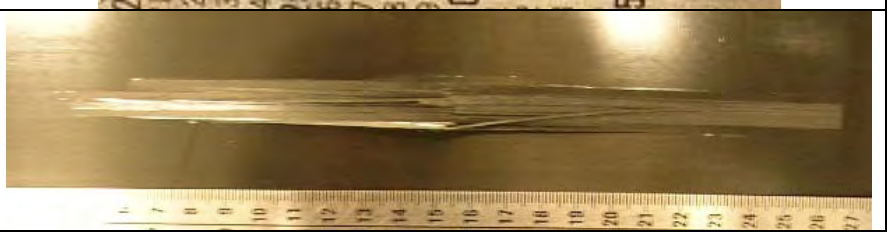

Figure 32. Sixteen-Ply Unidirectional Composite Panel Damage From Spheres

The panel damage characteristics are very similar to those of the 8-ply composites. High projectile velocities caused some shear plugging at the front of the panel, with breaking of fibers and localized delamination at the back. At mid-range speeds, the projectile broke the fibers at the point of impact and caused delamination along the fiber direction as it pushed its way through the panel. As before, delamination spread closer to the panel edge with decreasing speeds. At low velocities near the ballistic limit, there was very little fiber breakage or delamination. Instead, the panels fracture along the fiber direction starting from the point of impact.

3.5 ANGLE OF INCIDENCE.

The use of cylindrical projectiles resulted in some trouble due to tumbling of the projectile while in flight. An example of this tumbling, which is shown in figure 33, yielded inconsistent points of impact and different failure modes than expected. Especially with flat-ended cylinders, if the angle of incidence was too great, there would be tearing when shear plugging was expected. An example of this tearing is shown in figure 34.

Figure 33. Projectile Tumbling

Figure 34. Tearing Caused by a Tumbling Flat-Ended Cylinder

Pitch of the projectiles was measured for all cylindrically shaped projectiles (flat-ended and hemispherically ended) at the point of impact, and is plotted versus initial velocity in figure 35. Positioning of the camera did not allow for a measure of yaw. There appears to be no consistent relationship between initial velocity and angle, though it seems more likely to have extreme (greater than 10°) angle of incidence at low initial velocities.

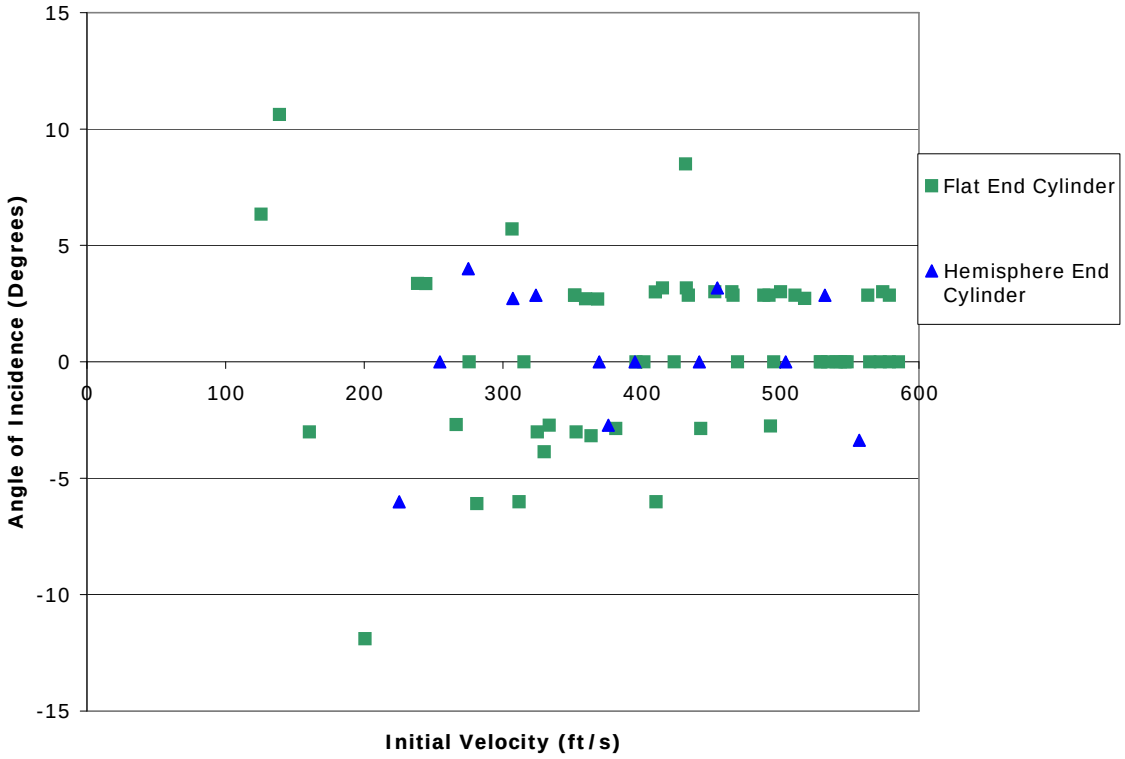

Figure 35. Angle of Incidence of the Cylindrical Projectile at Impact Versus Initial Projectile Velocity

3.6 INSTRON TESTING RESULTS.

Both alloy types of aluminum target plates were tested with both types of cylindrical projectiles; and an 8-ply composite plate was tested with a hemispherically ended projectile on the Instron machine. All combinations were tested three times to ensure consistency and that no additional plastic deformation was being caused by the testing. Load versus displacement curves for all tests are provided in appendix D, and a representative set of curves is shown in figure 36. Figure 36 contains results from a test of 2024-T3 aluminum with a flat-ended cylinder; the series number represents the order in which the three tests were performed. Note these plots are in Newtons (N) versus millimeters (mm).

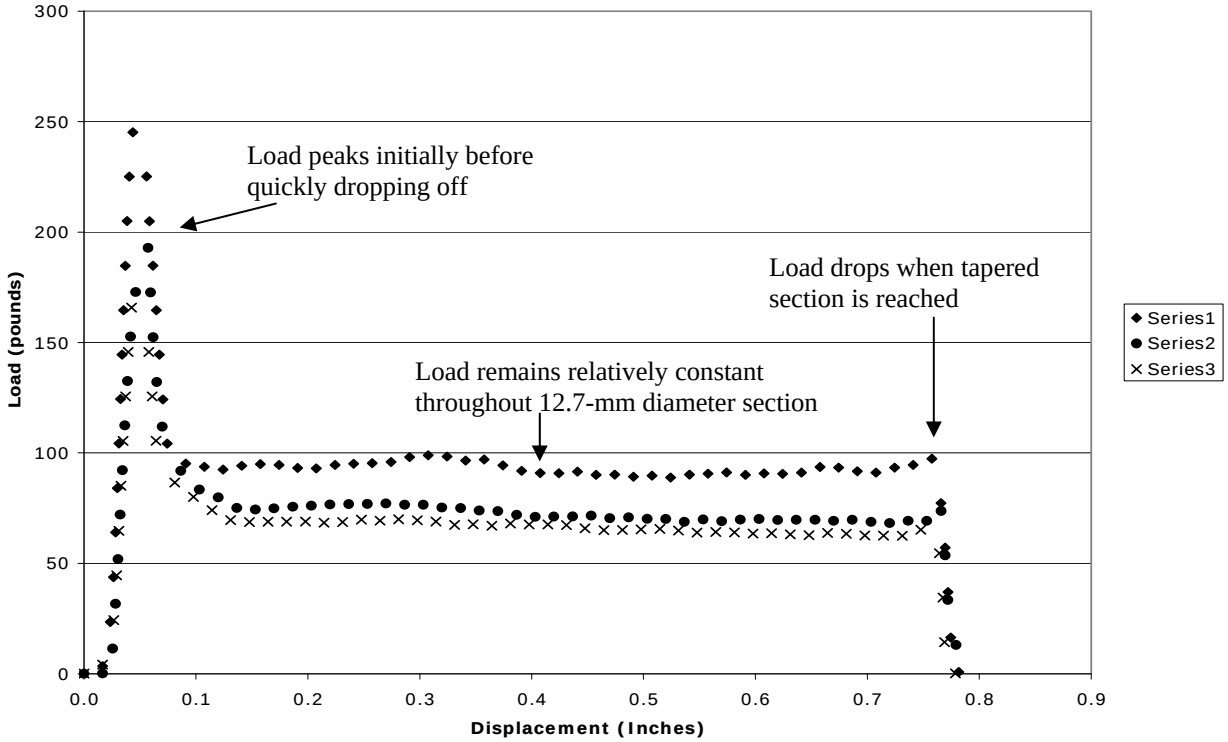

Figure 36. Load vs Displacement Curves From Instron Testing for 2024-T3 Aluminum With a Flat-Ended Cylinder

Of note, the first test of a set usually required slightly higher loads. This suggests some additional plastic deformation is taking place while the projectile is pushed through the target plate. The initial peak seen during the tests may be due to some issues with the alignment of the projectile with respect to the target plate.

4. ANALYSIS.

4.1 ENERGY ANALYSIS.

Knowing that work done equals change in projectile energy, ballistic curves can be predicted for all combinations of targets and projectile shapes. These predictions rely on the assumption that the change in energy is constant for a given combination. Initial projectile kinetic energy (KE) is equal to the sum of the work done and the residual projectile energy:

$$KE = \frac{1}{2} m v_i^2 = AE + \frac{1}{2} m v_r^2 \tag{1}$$

where m is the projectile mass, AE is the work done, v_i is the initial projectile velocity, and v_r is the residual projectile velocity. The ballistic limit occurs when the residual velocity of the projectile is zero:

$$v_{bl} = \sqrt{\frac{2AE}{m}} \tag{2}$$

where v_{bl} is the ballistic limit. Average energy losses, given in table 3, are used in equation 2, to predict ballistic limits, also shown in table 3.

Table 3. Predicted Ballistic Limits Based on the Assumption of Constant Projectile Energy Loss

Test Configuration	Average Projectile Energy Loss (J)	Average Projectile Energy Loss per Ply (J)	Predicted Ballistic Limit (ft/s)	Experimental Ballistic Limit (ft/s)
2024-T3 Sphere	61	N/A	397	394 ±5
2024-T3 Cylinder	107	N/A	250	250 ±5
2024-T3 Hemisphere	84	N/A	220	226 ±5
7075-T73 Sphere	98	N/A	502	492 ±5
7075-T73 Cylinder	144	N/A	289	289 ±5
7075-T73 Hemisphere	119	N/A	262	2764 ±5
8-ply Sphere	21	2.6	230	203 ±5
8-ply Hemisphere	24	3.0	118	115 ±5
16-ply Sphere	49	3.0	358	344 ±5
16-ply Hemisphere	54	3.4	177	171 ±5

J = Joules

Of note, average energy loss with hemispherically ended cylinder projectiles was approximately 20 joules higher than with spherical projectiles for both types of aluminum. Given the similarity of the failure mechanisms when using these projectiles, this suggests extra energy is required to push the cylindrical part of a projectile through the plate after initial penetration. The other two cylindrical projectiles also had significantly more energy loss than spherical projectiles. This energy may be expended to keep the hole elastically deformed and large enough for the projectile to pass through, and to overcoming friction between the projectile and target. It should

be noted that because there was a large difference in mass between the spherical and cylindrical projectiles (0.018 lb (8.3g) versus 0.082 lb (37.1g), respectively), the ballistic limits for the sphere were much higher than for the cylinders on the same target. This may have changed the failure mechanism affecting the energy loss also.

For the aluminums tested, the average energy loss using flat-ended cylinders was higher than when using hemispherically ended cylinders. This suggests that more energy is needed for penetration with shear plugging than for penetration with petalling. Although some of the extra energy loss may be due to the tearing associated with tumbling cylinders, those energy losses were included in the average.

As expected, the average energy loss for the 16-ply composites was greater than for the 8-ply composites. There does not seem to be as great a variation between average energy loss using different projectile types for composites. This is not surprising given the similarity between failure mechanisms using different projectiles. Also, average energy loss with hemispherically ended cylindrical projectiles was only slightly greater than with spherical projectiles, suggesting possibly that it is easier to continue pushing a projectile through broken and delaminated fibers than through petalled aluminum, or that the failure mechanism is affecting the results, or a combination of the two.

Rearranging the terms of equation 1 allows residual velocity to be calculated from initial velocity and average energy loss:

$$v_r = \sqrt{v_i^2 - \frac{2AE}{m}} \tag{3}$$

This yields predicted ballistic curves if the energy loss is assumed constant. Figures 37-46 show these predicted ballistic curves. All predicted curves, with the exception of figure 43 for 8-ply composites impacted with spheres, seem to fit quite well to the experimental data. It appears this exception could be because there was not enough test data taken near the ballistic limit. This suggests the validity of the constant projectile energy loss assumption for the other combinations.

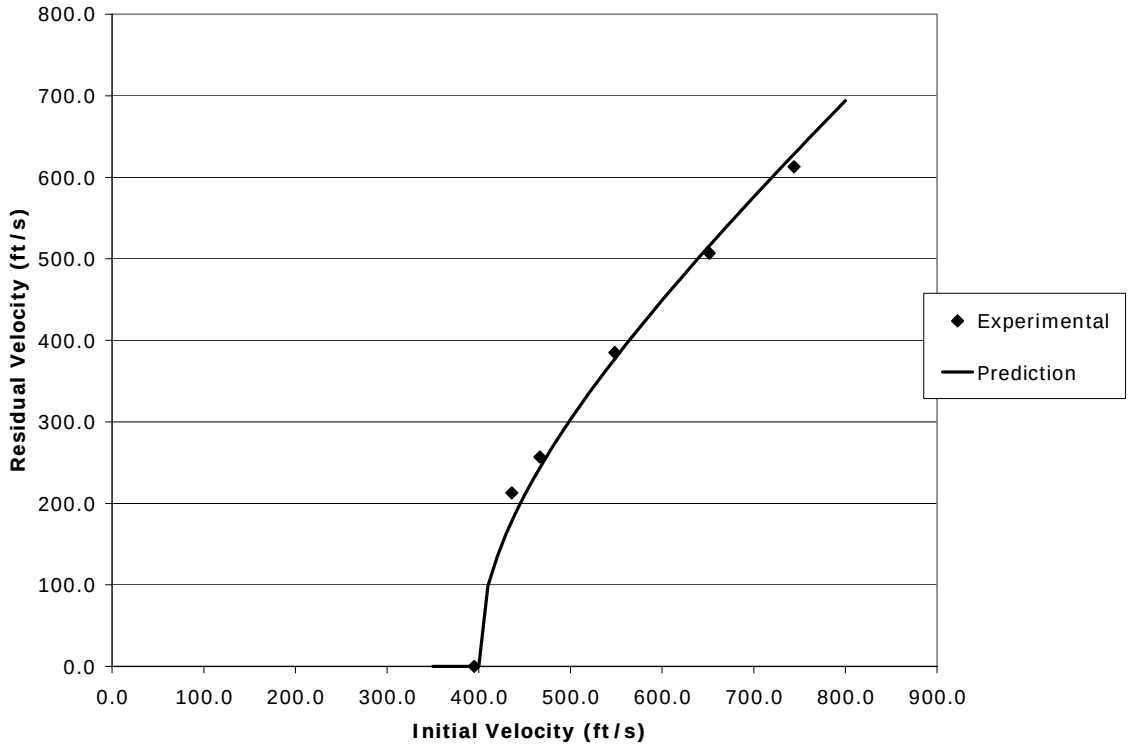

Figure 37. Predicted Impact Curve for 2024-T3 Aluminum With Spheres

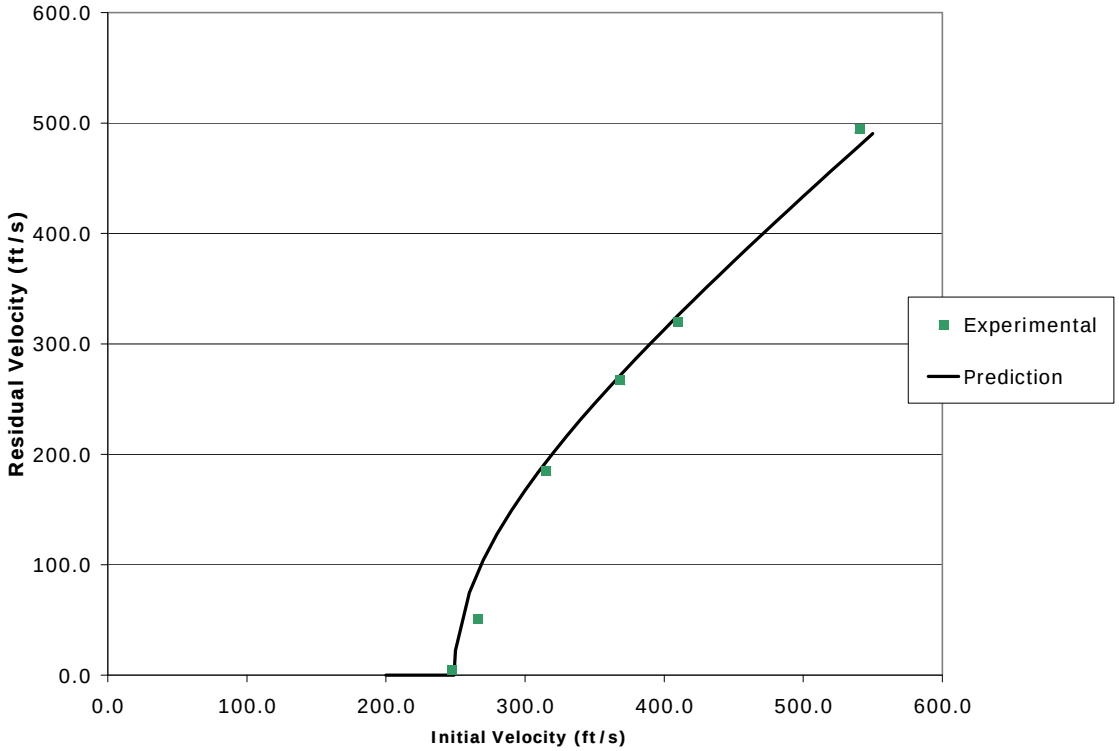

Figure 38. Predicted Impact Curve for 2024-T3 Aluminum Flat-Ended Cylinders

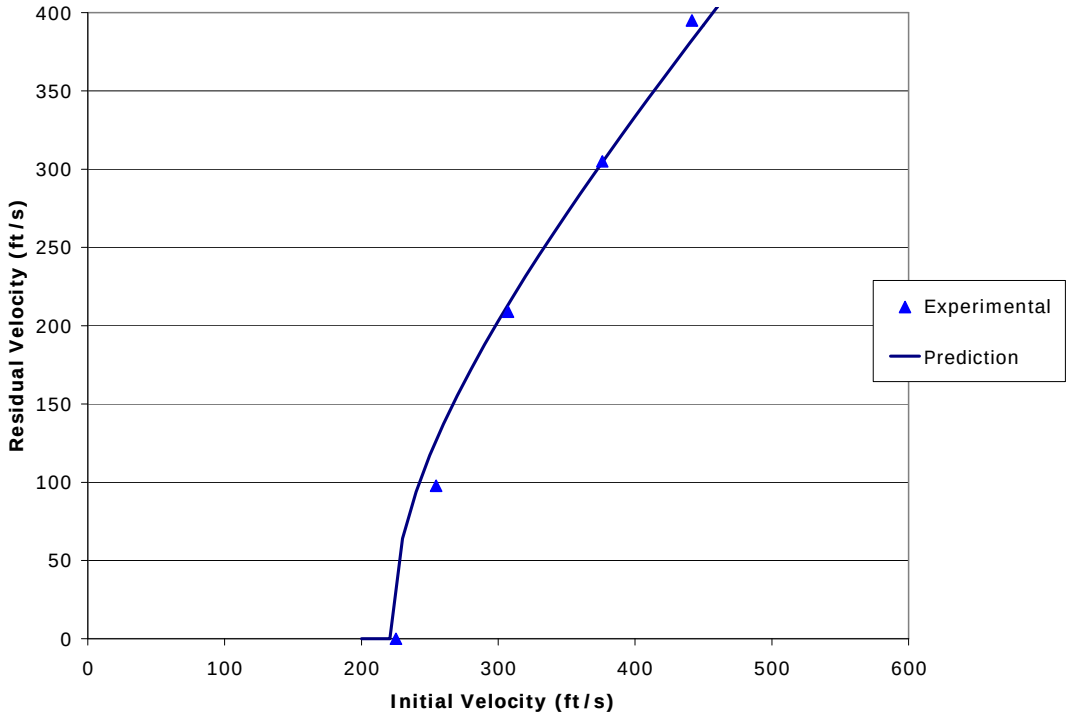

Figure 39. Predicted Impact Curve for 2024-T3 Aluminum With Hemispherically Ended Cylinders

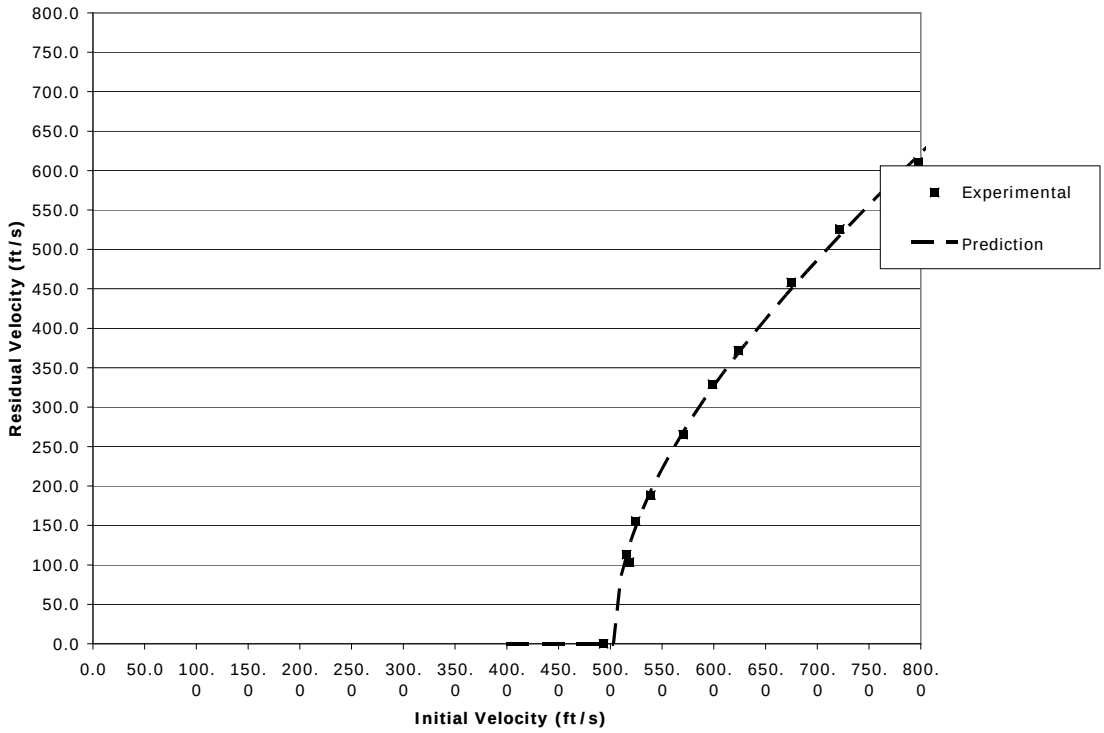

Figure 40. Predicted Impact Curve for 7075-T73 Aluminum With Spheres

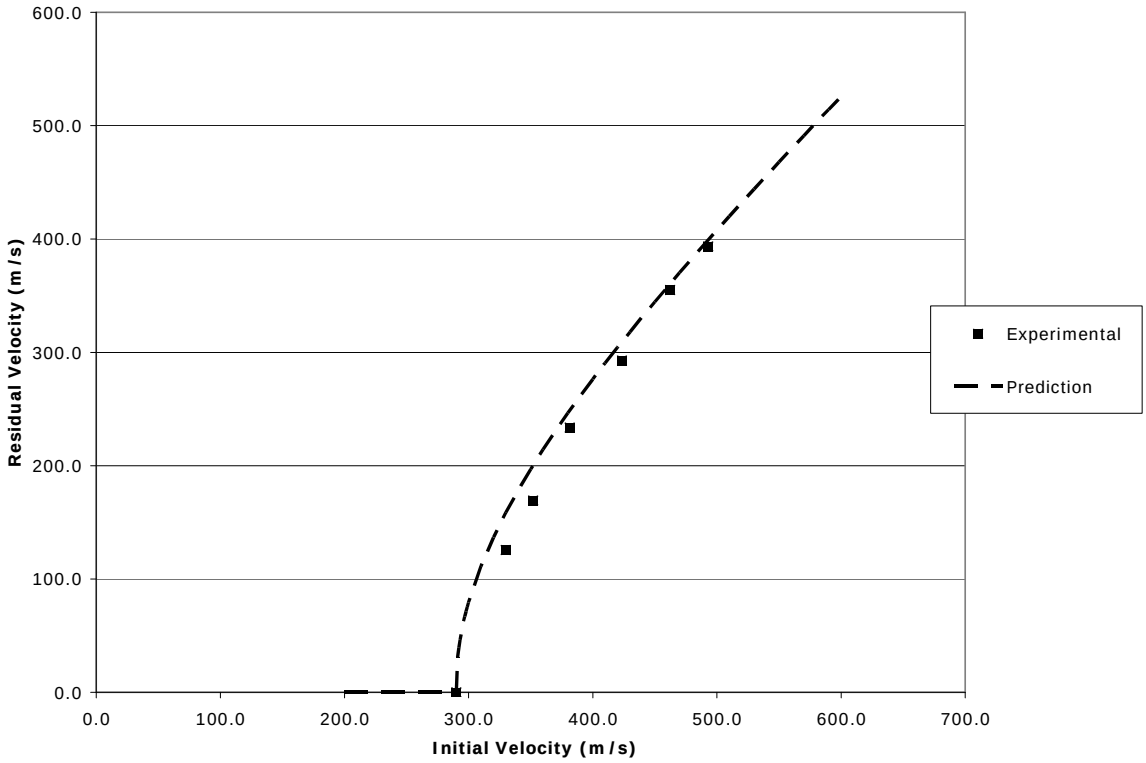

Figure 41. Predicted Impact Curve for 7075-T73 Aluminum With Flat-Ended Cylinders

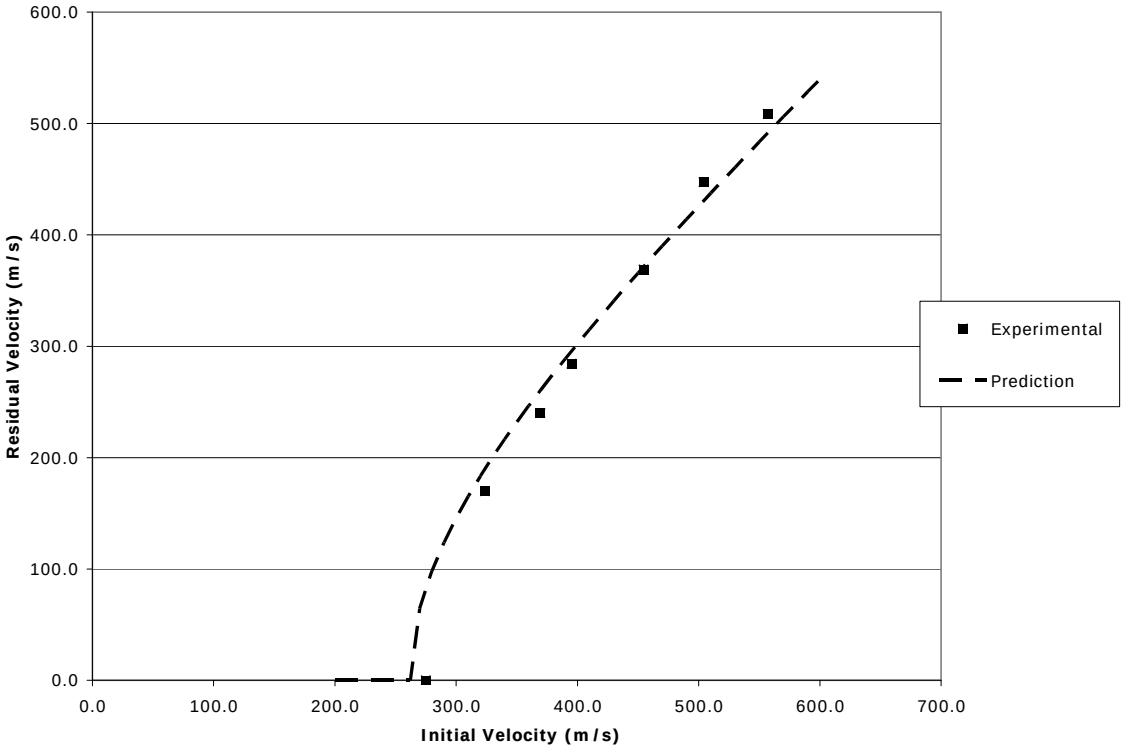

Figure 42. Predicted Impact Curve for 7075-T73 Aluminum With Hemispherically Ended Cylinders

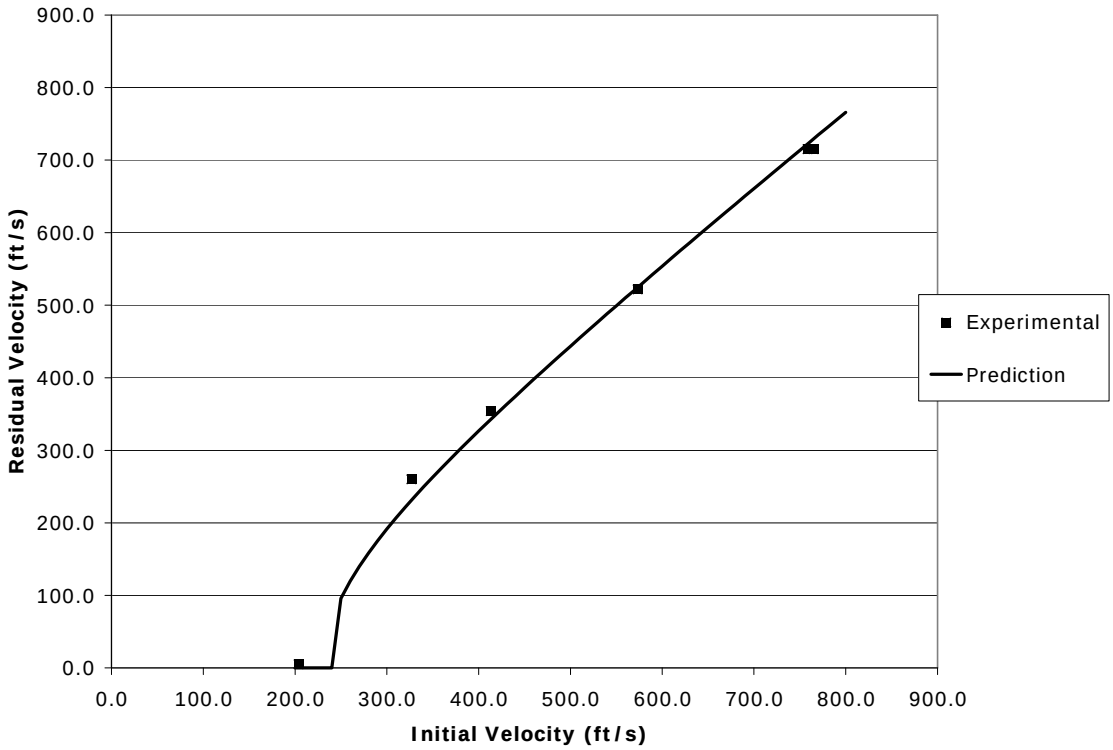

Figure 43. Predicted Impact Curve for 8-Ply Composite With Spheres

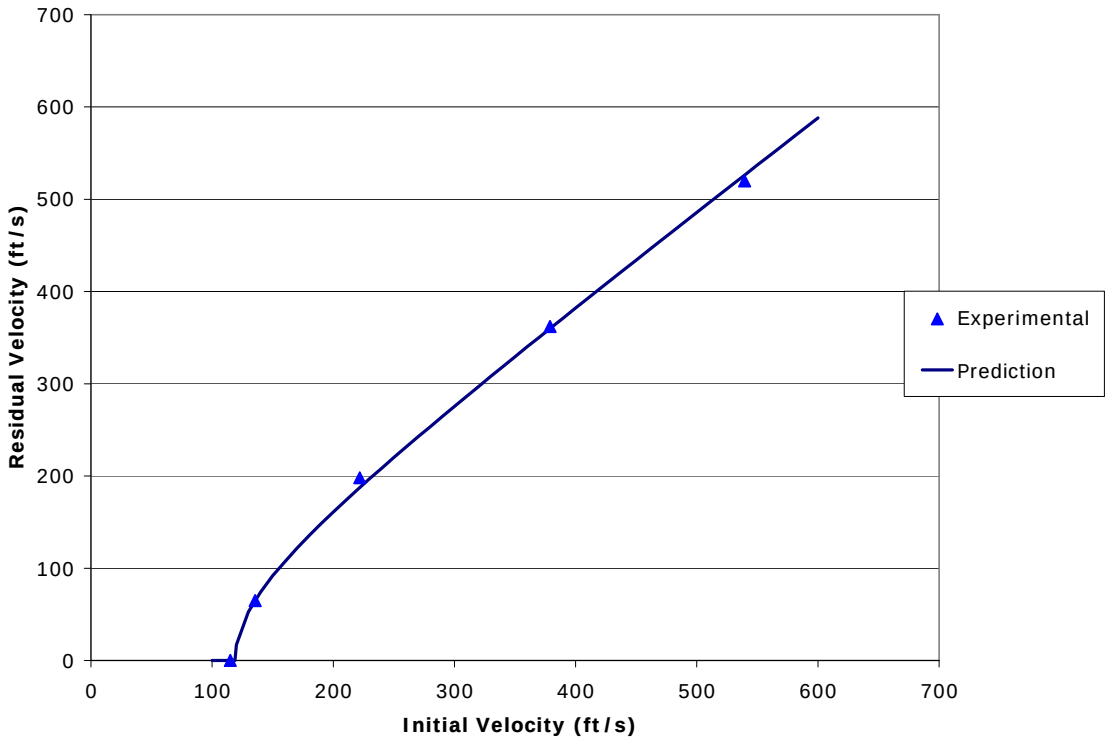

Figure 44. Predicted Impact Curve for 8-Ply Composite With Hemispherically Ended Cylinders

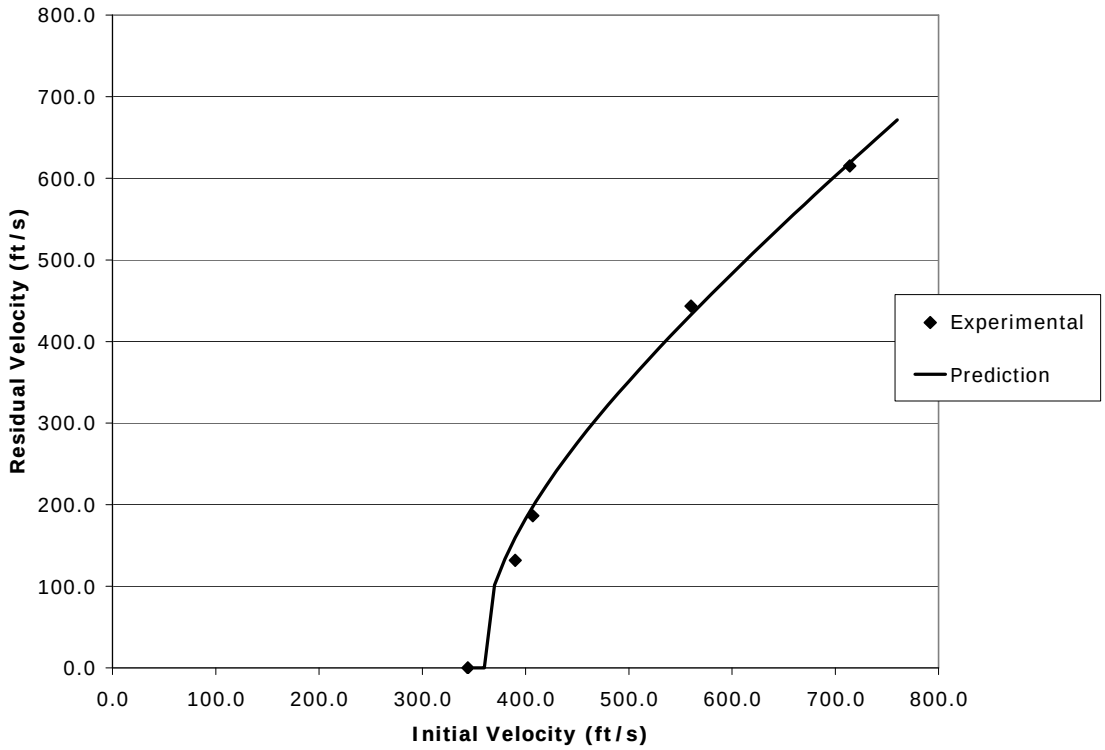

Figure 45. Predicted Impact Curve for 16-Ply Composite With Spheres

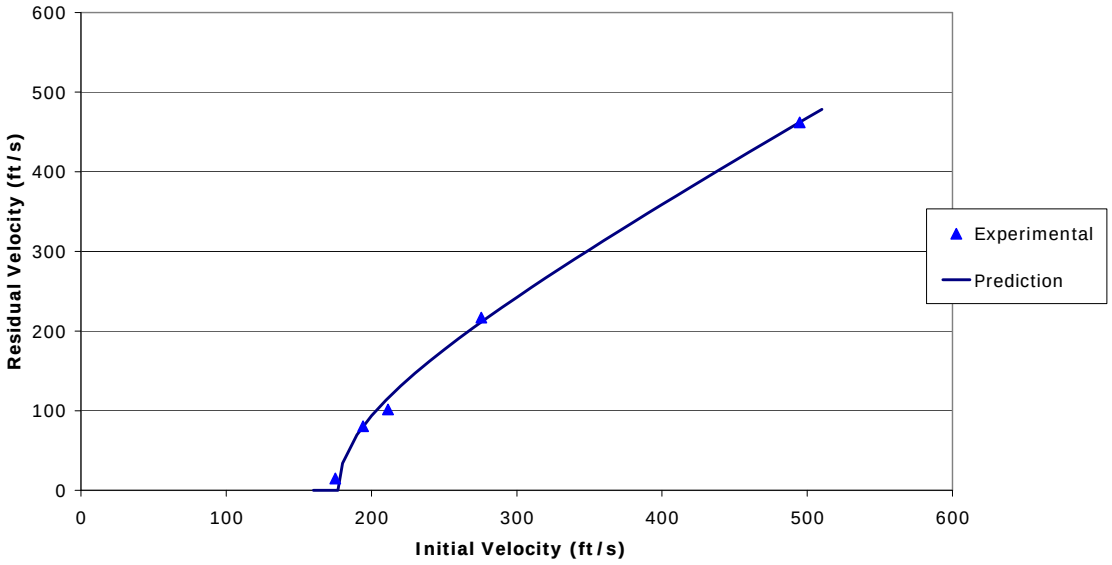

Figure 46. Predicted Impact Curve for 16-Ply Composite With Hemispherically Ended Cylinders

4.2 SHEAR PLUGGING ENERGY.

The energy required for flat-ended cylindrical projectiles to create a shear plug in the aluminum targets can be estimated with the help of equation 4 [4]:

$$K_c = \sqrt{EG_c} \tag{4}$$

where K_c is the material fracture toughness, E is Young's Modulus, and G_c is a measure of fracture energy. The work required to create a surface of area A is given in equation 5:

$$work = \frac{AG_c}{2} \tag{5}$$

Substituting equation 4 into equation 5, and taking the surface area created to be equal to the product of plate thickness and projectile circumference, yields:

$$work = \frac{\pi dtK_c^2}{E} \tag{6}$$

where d is projectile diameter 0.5 in. and t is target place thickness. The work required to create plugs in both types of aluminum is given in table 4.

Table 4. Estimated Work Required to Create Shear Plugs in Aluminums With Flat-Ended Cylinders

Alloy	Thickness, t (in.)	Fracture Toughness, K_c (MPa√m) [5]	Young's Modulus, E (GPa)	Work (J)
2024-T3	0.063	36	73.1	1.12
7075-T73	0.079	32	72	1.13

4.3 CYLINDER INSTRON TESTING.

The results of the Instron testing can be used to estimate the extra energy required to push a simulated cylindrical projectile through a target plate hole. This work done in pushing the projectile is approximately equal to the product of the average load required during testing and the length of the 1/2-inch-diameter section of an unmodified projectile. Note that only the first of three tests for each combination was used, and the initial peak observed during testing was not included in the averaging. Average loads and estimates of the energy required for pushing the projectile are shown in table 5.

Table 5. Estimated Work Required for Cylindrical Sections of Projectiles to Pass Through Target Plates

Test Configuration	Average Load (lb)	Work Required (J)
2024-T3 Cylinder	92.8	14
2024-T3 Hemisphere	85.4	11
7075-T73 Cylinder	158.5	24
7075-T73 Hemisphere	183.9	25
8-ply Hemisphere	11.0	1.5

The amount of work required for pushing hemispherically ended cylinders through the 8-ply composite is significantly less than pushing the hemispherically ended cylinders through the aluminums. This may explain why there is little difference in spherical and cylindrical projectile energy loss when composite targets are used. An average of about 20 J is required to push hemispherically ended cylinders through aluminum. This was the approximate difference in projectile energy loss between spheres and hemispherically ended cylinders.

5. CONCLUSIONS.

After experimentation and analysis of the results, the following conclusions have been reached:

- In the ballistic impact tests conducted in this study, both 2024-T3 and 7075-T73 aluminum alloy, spherical and hemispherically ended cylinder projectiles caused shear plugging followed by petalling, and flat-ended cylinders cause shear plugging but little or no petalling. Plug size increased with increasing projectile velocity and increasing area of the point of impact.

- For 8- and 16-ply unidirectional composites tested, high projectile velocity caused shear plugging at the front of the panel with fiber breakage and localized delamination along the fiber direction at the back, mid-range projectile velocity causes fiber breakage and delamination along the fiber direction at both the front and back of the panel, and low projectile velocity caused fracture along the fiber direction with little fiber breakage or delamination.

- There appeared to be no strong relationship between initial projectile velocity and angle of incidence for cylindrical projectiles in the ballistic impact tests of this study.

- For both aluminum alloys tested in quasi-static tests, hemispherically and flat-ended cylindrical projectiles required a greater amount of energy to pass through a target plate than spherical projectiles. This energy may be expended to keep the hole elastically deformed and large enough for the projectile to pass through and to overcome friction between the projectile and plate. No impact data was obtained during this study with varying length projectiles of the same tip shape to compare energy loss. This type of testing could be used to verify the Instron machine quasi-static test results.

- For both unidirectional composites, projectile shape did not seem to greatly influence the amount of energy required to pass through a panel.

- The assumption of constant projectile energy loss appears valid and could be useful in predicting ballistic curves and limits.

6. REFERENCES.

1. Phantom High Speed Digital Imaging by Vision Research, Inc., retrieved May 16, 2006, from http://visiblesolutions.com/

2. Aluminum 2024-T3, retrieved May 8, 2006, from http://matweb.com/search/Specific Material.asp?bassnum=MA2024T3

3. Aluminum 7075-T73; 7075-T735x, retrieved May 8, 2006, from http://matweb.com /search/SpecificMaterial.asp?bassnum=MA7075T73

4. Barret, Craig R., Nix, William D., and Tetelman, Alan S., *The Principles of Engineering Materials*, New Jersey, Prentice-Hall, Inc., 1973.

5. Kaufman, J. Gilbert, Aluminum Alloy Database, Knovel Corp., NY, 2004, Retrieved May 24, 2006, from http://www.knovel.com/knovel2/Toc.jsp?BookID=844

APPENDIX A—CAMERA INSTRUCTIONS

A.1 INITIAL SETUP.

1. A white background is placed behind the projectile path, and a 0.5-inch-diameter section of drill rod is placed in the pneumatic gun barrel. There are two pieces of tape 6 inches apart on the rod.

2. The high-intensity lamps are turned on.

3. In the Phantom Camera Control Window, under the "Acquisition" menu, "Setup and Recording" is clicked.

4. Under "Resolution," 256 x 64" is clicked.

5. The camera position is adjusted until the desired field of view is acquired and the drill rod appears horizontal.

6. The zoom, focus, and aperture on the camera lens are adjusted until the rod appears sharp.

7. "Adjust" is clicked, and "Brightness," "Contrast," and "Gamma" are adjusted until a clear image is acquired.

8. "Options" is clicked followed by "Black Reference." The lens cover is placed on the lens, and "OK" is clicked followed by "No." The camera lens is removed.

9. The camera is triggered.

10. "OK" is clicked to open the "View Cine" window.

11. "Mark Begin" is clicked.

12. The video is advanced five frames.

13. "Mark End" is clicked.

14. Save is clicked to save the video.

15. "Measure" is clicked followed by "Units." Distance is set to "inches" and speed to "feet per second."

16. "Measure" is clicked followed by "Scaling." A 6-inch measurement is entered in the box that appears.

17. The left edge of the left-most piece of tape is clicked followed the left edge of the right-most piece of tape. The camera is calibrated until the program is closed.

A.2 RECORDING A TEST.

1. In Phantom Camera Control Window, under the "Acquisition" menu, "Setup and Recording" is clicked.

2. Sample rate is set to 10,000 frames per second, exposure time to 20 μs, EDR Exposure to 0 μs, and Post Trigger to 24480 p.

3. "Cont. rec…" is clicked follow by "Close." "Waiting for Trigger" should be displayed in the lower portion of the screen.

4. The pneumatic gun is triggered as described in the Experimental Procedure.

5. "OK" is clicked to open the "View Cine" window.

6. The "Play" button is clicked, and when the projectile appears on screen, "Pause" is clicked.

7. The video is advanced until the projectile leaves the field of view, and "Mark End" is clicked.

8. The video is rewound until the frame before the projectile enters the screen, and "Mark Begin" is clicked.

9. "Save" is clicked to save the video for analysis.

A.3 DETERMINING RESIDUAL VELOCITY.

1. Projectile has exited to the target.

2. "Measure" is clicked and "Distance and Speed" is selected, followed by "2 points."

3. The center of the projectile is clicked.

4. The video is advanced to the last frame before the projectile begins to exit the field of view.

5. The "Center of the Projectile" is clicked, and Distance Traveled" as well as "Velocity" are displayed in the lower portion of the screen.

A.4 DETERMINING RESIDUAL ANGLE OF INCIDENCE.

1. In the "View Cine" window, the video is advanced to the final frame before the projectile enters the target.

2. "Measure" is clicked and "Angle and Angular Speed" is selected, followed by "2 points."

3. The right end of the projectile is clicked.

4. The left end of the projectile is clicked and angle of incidence is displayed in the lower portion of the screen.

APPENDIX B—IMPACT DATA

Table B-1. Aluminum 0.063-in. (1.59-mm) 2024-T3 With Spheres

Mass (g)	Initial Velocity in./sec (m/s)	Residual Velocity in./sec (m/s)	Initial Energy (J)	Final Energy (J)	Energy Loss (J)
8.3	744.1 (226.8)	612.9 (186.8)	213.4	144.9	68.5
8.3	651.6 (198.6)	506.9 (154.5)	163.6	99.1	64.5
8.3	548.2 (167.1)	384.8 (117.3)	115.9	57.1	58.7
8.3	466.5 (142.2)	256.9 (78.3)	83.9	25.5	58.5
8.3	395.0 (120.4)	0.0 (0.0)	60.2	0.0	60.2
8.3	436.0 (132.9)	212.9 (64.9)	73.3	17.5	55.8

Table B-2. Aluminum 0.063-in. (1.59-mm) 2024-T3 With Flat-Ended Cylinders

Mass (g)	Initial Velocity in./sec (m/s)	Residual Velocity in./sec (m/s)	Initial Energy (J)	Final Energy (J)	Energy Loss (J)	Angle (deg)
37.1	540.4 (164.7)	495.0 (150.9)	503.3	422.3	81.0	0.0
37.1	315.3 (96.1)	185.0 (56.4)	171.2	59.0	112.2	0.0
37.1	410.1 (125.0)	319.9 (97.5)	289.7	176.5	113.2	3.0
37.1	266.4 (81.2)	50.9 (15.5)	122.2	4.5	117.7	-2.7
37.1	368.4 (112.3)	267.1 (81.4)	234.0	122.9	111.1	2.7
37.1	247.7 (75.5)	4.9 (1.5)	105.8	0.0	105.7	5.7

Table B-3. Aluminum 0.063-in. (1.59-mm) 2024-T3 With Hemispherically Ended Cylinders

Mass (g)	Initial Velocity in./sec (m/s)	Residual Velocity in./sec (m/s)	Initial Energy (J)	Final Energy (J)	Energy Loss (J)	Angle (deg)
37.1	532.2 (162.2)	462.9 (140.8)	488.0	367.8	120.1	2.9
37.1	376.0 (114.6)	305.1 (93.0)	243.6	160.3	83.3	-2.7
37.1	307.1 (93.6)	209.0 (63.7)	162.6	75.3	87.4	2.7
37.1	254.6 (77.6)	97.8 (29.8)	111.7	16.5	95.2	0.0
37.1	225.4 (68.7)	0.0 (0.0)	87.4	0.0	87.4	-6.0
37.1	441.6 (134.6)	395.0 (120.4)	336.0	268.9	67.1	0.0

Table B-4. Aluminum 0.079-in. (2-mm) 7075-T73 With Spheres

Mass (g)	Initial Velocity in./sec (m/s)	Residual Velocity In./sec (m/s)	Initial Energy (J)	Final Energy (J)	Energy Loss (J)
8.3	797.2 (243.0)	610.9 (186.2)	245.1	143.8	101.2
8.3	674.9 (205.7)	458.3 (139.7)	175.5	81.0	94.6
8.3	623.7 (190.1)	371.4 (113.2)	150.0	53.2	96.8
8.3	524.6 (159.9)	155.8 (47.5)	106.1	9.4	96.8
8.3	493.4 (150.4)	0.0 (0.0)	93.9	0.0	93.9
8.3	570.2 (173.8)	265.1 (80.8)	125.4	27.1	98.3
8.3	721.8 (220.0)	525.9 (160.3)	200.8	106.7	94.2
8.3	518.4 (158.0)	103.3 (31.5)	103.6	4.1	99.5
8.3	814.0 (248.1)	627.6 (191.3)	255.5	151.8	103.7
8.3	539.4 (164.4)	188.6 (57.5)	112.1	13.7	98.4
8.3	598.8 (182.5)	329.1 (100.3)	138.3	41.7	96.5
8.3	515.7 (157.2)	112.9 (34.4)	102.5	4.9	97.6

Table B-5. Aluminum 0.079-in. (2-mm) 7075-T73 With Flat-Ended Cylinders

Mass (g)	Initial Velocity in./sec (m/s)	Residual Velocity in./sec (m/s)	Initial Energy (J)	Final Energy (J)	Energy Loss (J)	Angle (deg)
37.1	236.2 (72.0)	0.0 (0.0)	564.2	517.5	46.7	0.0
37.1	572.2 (174.4)	539.0 (164.3)	96.3	0.0	96.3	n/a
37.1	493.1 (150.3)	393.3 (119.9)	418.9	266.7	152.1	-2.8
37.1	423.6 (129.1)	292.7 (89.2)	309.1	147.7	161.4	0.0
37.1	352 (107.3)	169.3 (51.6)	213.5	49.4	164.1	2.9
37.1	329.7 (100.5)	125.7 (38.3)	187.4	27.2	160.2	-3.9
37.1	381.6 (116.3)	233.6 (71.2)	250.7	94.1	156.6	-2.9
37.1	462.3 (140.9)	255.0 (108.2)	368.4	217.2	151.2	180.0
37.1	290.0 (88.4)	0.0 (0.0)	144.9	0.0	144.9	0.0

Table B-6. Aluminum 0.079-in. (2-mm) 7075-T73 With Hemispherically Ended Cylinders

Mass (g)	Initial Velocity in./sec (m/s)	Residual Velocity in./sec (m/s)	Initial Energy (J)	Final Energy (J)	Energy Loss (J)	Angle (deg)
37.1	557.0 (169.8)	508.5 (155.0)	534.7	445.9	88.7	-3.4
37.1	454.4 (138.5)	369.0 (112.5)	356.0	234.7	121.4	3.2
37.1	323.8 (98.7)	169.9 (51.8)	180.7	49.8	130.9	2.9
37.1	369.3 (112.6)	240.2 (73.2)	235.2	99.3	135.9	0.0
37.1	274.9 (83.8)	0.0 (0.0)	130.4	0.0	130.4	4.0
37.1	503.9 (153.6)	447.5 (136.4)	437.6	345.1	92.5	0.0
37.1	395.3 (120.5)	284.4 (86.7)	269.2	139.3	129.9	0.0

Table B-7. Eight-Ply Unidirectional Composites With Spheres

Mass (g)	Initial Velocity in./sec (m/s)	Residual Velocity in./sec (m/s)	Initial Energy (J)	Final Energy (J)	Energy Loss (J)
8.3	758.5 (231.2)	714.9 (217.9)	221.8	197.1	24.6
8.3	764.8 (233.1)	714.9 (217.9)	225.5	197.1	28.4
8.3	413.4 (126.0)	354.0 (107.9)	65.9	48.3	17.5
8.3	326.8 (99.6)	259.8 (79.2)	41.2	26.1	15.1
8.3	203.7 (62.1)	4.92 (1.5)	16.0	0.0	16.0
8.3	573.2 (174.7)	522.0 (159.1)	126.7	105.1	21.6

Table B-8. Eight-Ply Unidirectional Composites With Hemispherically Ended Cylinders

Mass (g)	Initial Velocity in./sec (m/s)	Residual Velocity in./sec (m/s)	Initial Energy (J)	Final Energy (J)	Energy Loss (J)	Angle (deg)
37.1	539.4 (164.4)	520.0 (158.5)	501.4	466.0	35.4	-3.0
37.1	221.8 (67.6)	198.2 (60.4)	84.9	67.6	17.3	-2.7
37.1	135.5 (41.3)	65.0 (19.8)	31.7	7.3	24.4	-2.9
37.1	378.9 (115.5)	361.9 (110.3)	247.5	225.8	21.7	8.0
37.1	115.2 (35.1)	0.0 (0.0)	22.8	0.0	22.8	0.0

Table B-9. Sixteen-Ply Unidirectional Composites With Spheres

Mass (g)	Initial Velocity in./sec (m/s)	Residual Velocity in./sec (m/s)	Initial Energy (J)	Final Energy (J)	Energy Loss (J)
8.3	713.9 (217.6)	615.2 (187.5)	196.6	145.8	50.7
8.3	560.0 (170.7)	433.2 (135.1)	121.0	75.8	45.2
8.3	407.2 (124.1)	186.4 (56.8)	63.9	13.4	50.5
8.3	390.1 (118.9)	131.6 (40.1)	58.6	6.7	52.0
8.3	344.2 (104.9)	0.0 (0.0)	45.7	0.0	45.7

Table B-10. Sixteen-Ply Unidirectional Composites With Hemispherically Ended Cylinders

Mass (g)	Initial Velocity in./sec (m/s)	Residual Velocity in./sec (m/s)	Initial Energy (J)	Final Energy (J)	Energy Loss (J)	Angle (deg)
37.1	494.8 (150.8)	461.9 (140.8)	421.9	367.8	54.1	0.0
37.1	275.6 (84.0)	216.9 (66.1)	130.9	81.2	49.7	3.0
37.1	211.3 (64.4)	101.7 (31.0)	77.0	17.8	59.2	-7.8
37.1	194.2 (59.2)	80.3 (24.5)	65.0	11.2	53.8	0.0
37.1	175.2 (53.4)	15.1 (4.6)	52.8	0.4	52.4	0.0

THE BOEING COMPANY

Table 2.2.2-1 Ply Properties ⑥

TABLE: 2.2.2-1	PLY PROPERTIES
Prepreg Material Specicification:	BMS 8-212, TYPE III CLASS 1 or 3, GRADE 145 or 190
Resin Content:	37 (% WT)
Cured Ply Thickness:	0.0059 (in) - GRADE 145 0.0080 (in) - GRADE 190
Density:	0.056 lb/in^3
Process Specification:	BAC 5317-1

PROPERTY		UNIT	ENVIRONMENTAL CONDITION					
			-75° F		70° F		180° F ⑤	
			DRY	WET	DRY	WET	DRY	WET
MODULUS ②	E_1 ①	Msi	← 17.1 →					
	E_2	Msi			1.28			
	G_{12}	Msi	0.82		0.66			0.54
	G_{13}	Msi	0.82		0.66			0.54
	G_{23}	Msi	0.82		0.66			0.54
POISSON'S RATIO	ν_{12}	----	← 0.34 →					
COEFFICIENTS OF LINEAR THERMAL EXPANSION ③	α_1	in/in °F	$.02 \times 10^{-6}$				$.02 \times 10^{-6}$	
	α_2	in/in °F	15×10^{-6}				15×10^{-6}	
COEFFECIENTS OF LINEAR MOISTURE EXPANSION ④	β_1	in/in %M						
	β_2	in/in %M						
THERMAL CONDUCTIVITY	K_1	BTU/(hr ft °F)						
	K_2	BTU/(hr ft °F)						
	K_3	BTU/(hr ft °F)						

① E_1 is the average of tension and compression modull. For special analyses use tension/compression modulus adjustment factors to determine tension or compression E_1.

② Modulus values are secant values at a strain level of 4000 μ in/in. For special analysis use modulus versus strain curves to determine secant values at the desired strain level.

③ Values are for expansion between -75° F and 70° F, and 70° F and 180° F.

④ %M = Percent absorbed moisture by weight.

⑤ 180°F values are to be used for 160°F environment.

DG-100-531

⑥ Approved for public release

APPENDIX D—LOAD-DISPLACEMENT CURVES FROM INSTRON TESTS

Each combination was tested three times using the same target plate and projectile (figures D-1 through D-5). The series number in the legend indicates the order of the tests (with Series 1 being the first run).

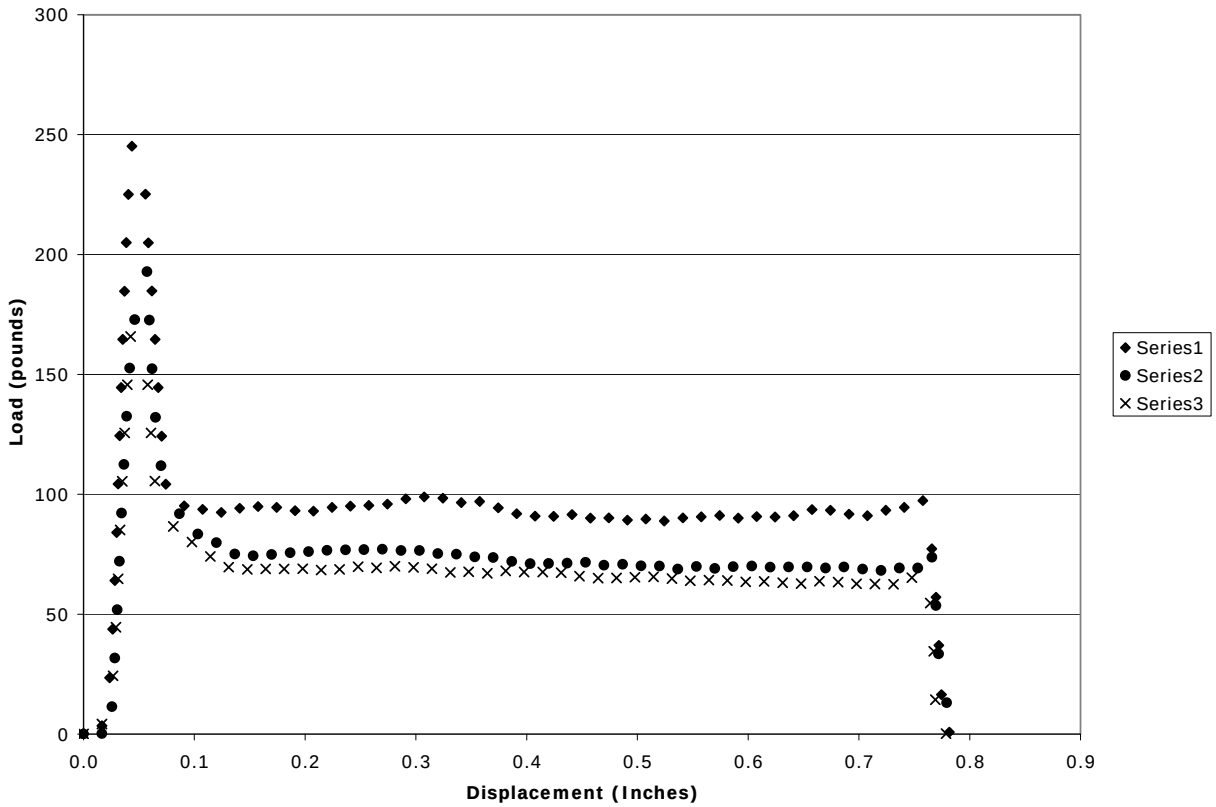

Figure D-1. Aluminum 1/16-Inch 2024-T3 With Flat-Ended Cylinders

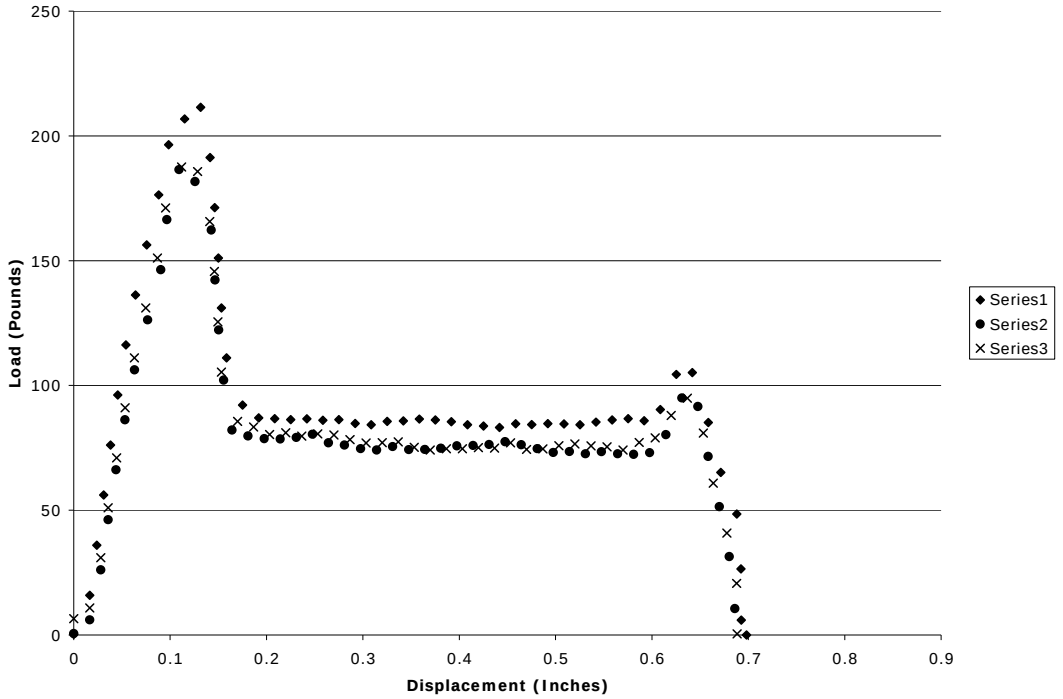

Figure D-2. Aluminum 1/16-Inch 2024-T3 With Hemispherically Ended Cylinders

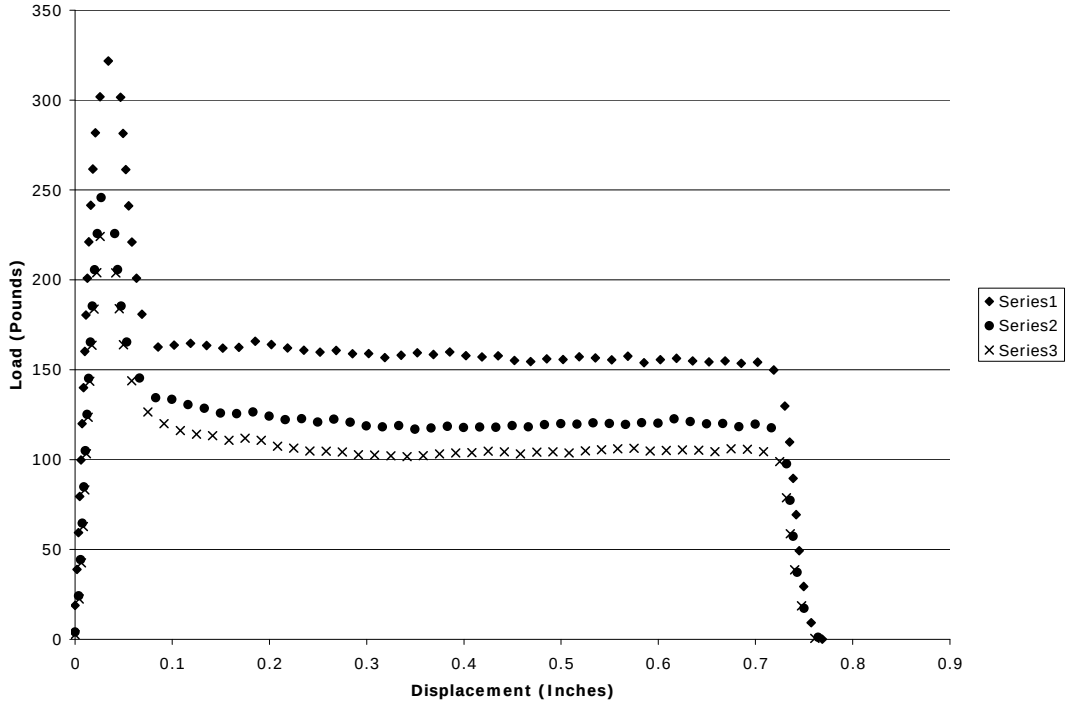

Figure D-3. Aluminum 5/64-Inch 7075-T73 With Flat-Ended Cylinders

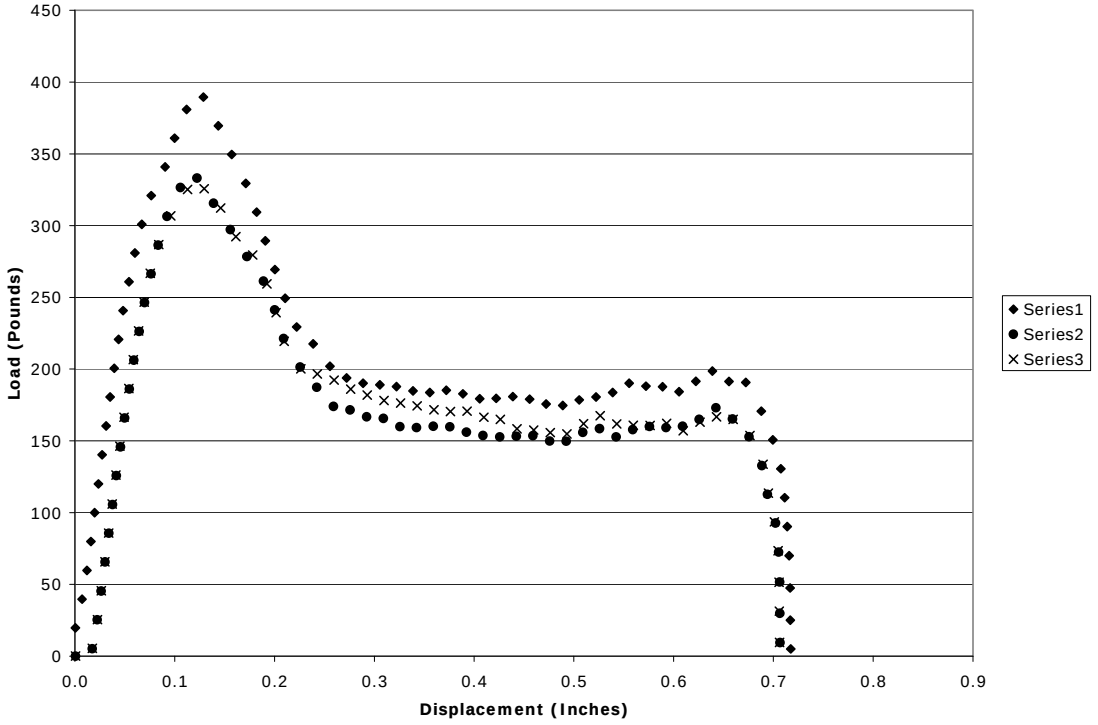

Figure D-4. Aluminum 5/64-Inch 7075-T73 With Hemispherically Ended Cylinders

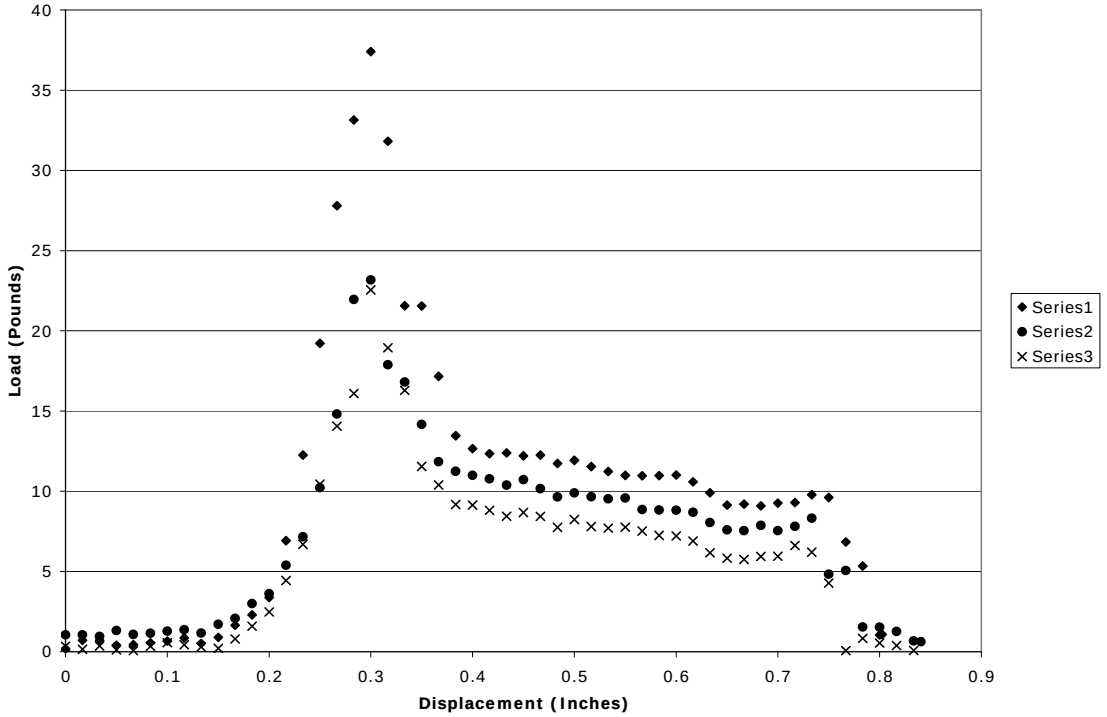

Figure D-5. Eight-Ply Unidirectional Composite With Hemispherically Ended Cylinders